ADVANCED MATERIALS
www.advmat.de

Engineered Plasmonic and Fluorescent Nanomaterials for Biosensing, Motion, Imaging, and Therapeutic Applications

David Esporrín-Ubieto, Juan C. Fraire, Daniel Sánchez-deAlcázar, and Samuel Sánchez**

The field of nanophotonics has seen remarkable advances, with gold-based materials standing out. By precisely fine-tuning the size and shape of metal nanoparticles (NPs), such as gold nanoparticles (AuNPs), it has been possible to gain control over light interaction, modulating localized surface plasmon resonance (LSPR), a phenomenon that involves the collective oscillation of free conduction electrons. This has opened the path toward more powerful biomedical applications, including surface-enhanced Raman spectroscopy (SERS) and photothermal therapy (PTT). When AuNPs dimensions fall below 2 nm, they become gold nanoclusters (AuNCs), losing the LSPR but acquitting fluorescence due to their molecule-like behavior. This unique feature makes them ideal for high-resolution imaging, biomarker detection, and advanced therapies. Beyond traditional uses, the recent inclusion of AuNPs into nanomotors (NMs) enhances precise in vivo tracking and targeted drug delivery. This review highlights the different applications of plasmonic nanomaterials with particular emphasis on AuNPs and AuNCs as a function of their shapes, sizes, and stabilization ligands. Moreover, it dives into the biosensing applications of plasmonic materials by addressing their so-called far-field and near-field optical properties, giving a detailed overview of different high-sensitivity immunoassays and biosensing. A comprehensive outlook on the evolution of plasmonic-based materials for the next therapies is provided.

1. Introduction

Nanotechnology, and in particular nanomedicine, has advanced rapidly in recent years, surpassing the boundaries of conventional medicine. This discipline focuses on studying materials with at least one dimension ranging from 1 to 100 nm, whose properties are inherently dependent on their size and shape.[1] In fact, inorganic nanomaterials are highly appealing for their durability, high contrast, and light-interaction properties.[2] Since Faraday's[3] discovery of gold nanoparticles (AuNPs) dispersions in the 1850s, scientists have developed precise synthesis methods to tailor their properties for specific applications.

Among all inorganic elements, gold and silver stand out for their exceptional photonic properties when structured into nanoparticles (NPs).[4,5] When electromagnetic (EM) radiation interacts with metallic NPs whose spatial dimensions are significantly smaller than the wavelength of the incident field, the conduction electrons within the metal become polarized, resulting in the formation of polarization charges at the particle surface. The electrostatic attraction exerted by the positively charged ion cores acts as a restoring force, inducing a standing-wave-like coherent oscillation of the electrons in the conduction band. This collective excitation of electrons is termed a plasmonic oscillation, and specifically, when it arises from the coupling of light with the NPs, is referred to as localized surface plasmon resonance (LSPR). NPs (e.g., gold nanospheres) exhibit an LSPR that depends on their size and composition, while 1D nanostructures (e.g., gold nanorods, nanowires) also show LSPR modes, often split into transverse and longitudinal resonances.[6,7]

In this review, we first explore how the shape and morphology of AuNPs influence their optical properties and light interactions, directly impacting their biomedical applications.[8] As the optical properties of the colloidal system will depend upon the degree of plasmon coupling of the NPs that integrate it, we also examine how the choice of ligands plays a crucial role in enhancing aqueous dispersion stability and enabling intelligent aggregation under specific environmental conditions.[9,10] Furthermore, we present the emerging role of AuNPs in nanomotors (NMs), where their integration enhances active matter technology and enables precise in vivo tracking via advanced imaging.[11] Additionally, AuNP-functionalized NMs expand therapeutic applications, notably in photothermal therapy (PTT). In this approach, AuNPs efficiently absorb near-infrared (NIR) light and convert it

D. Esporrín-Ubieto, J. C. Fraire, D. Sánchez-deAlcázar[+], S. Sánchez
Institute for Bioengineering of Catalonia (IBEC)
Barcelona Institute of Science and Technology (BIST)
Baldiri i Reixac 10-12, Barcelona 08028, Spain
E-mail: desporrin@ibecbarcelona.eu; ssanchez@ibecbarcelona.eu
S. Sánchez
Institució Catalana de Recerca i Estudies Avancats (ICREA)
Passeig Lluís Companys 23, Barcelona 08010, Spain

The ORCID identification number(s) for the author(s) of this article can be found under https://doi.org/10.1002/adma.202502171

[+]Present address: Nanobots Therapeutics SL, Baldiri i Reixac 4, 08028 Barcelona, Spain

DOI: 10.1002/adma.202502171

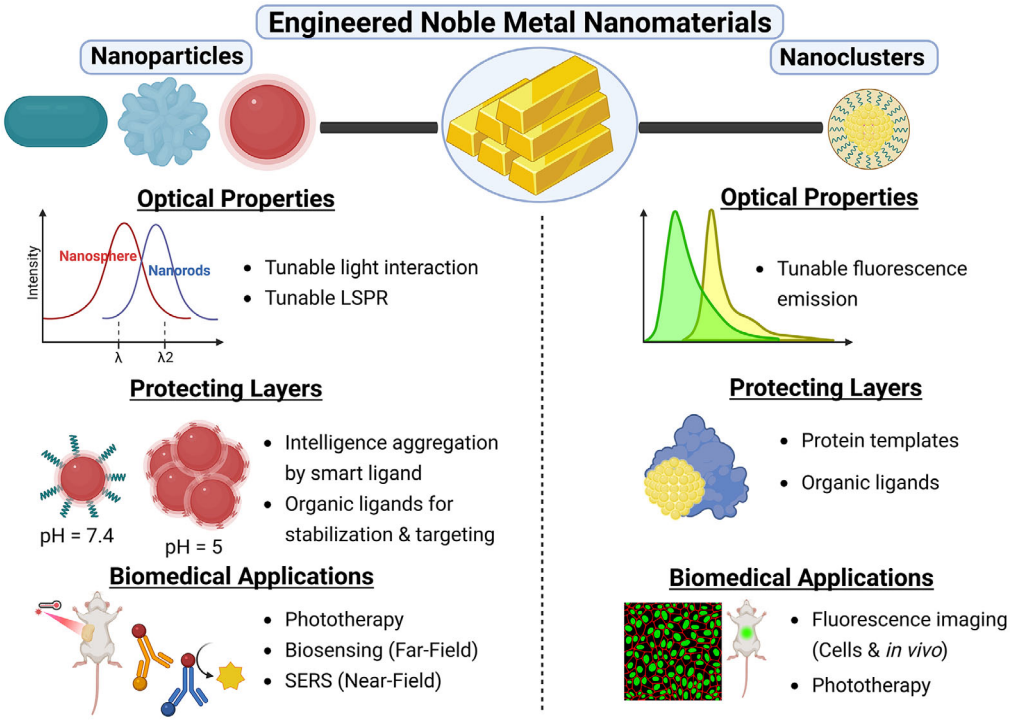

Figure 1. The scheme shows the main properties and applications of noble metal nanoparticles (NPs) and nanoclusters (NCs). Created in BioRender. Sánchez, S. (2025) https://BioRender.com/bw9zqrd.

into highly localized heat, enabling the targeted ablation of pathological tissues, including tumors, with minimal invasiveness.[12]

We explored the optical behavior of plasmonic NPs, distinguishing between far-field and near-field effects.[13] Far-field interactions govern light absorption and scattering, enhancing contrast in imaging techniques such as fluorescence microscopy and optical coherence tomography. In contrast, near-field effects generate localized EM hotspots, dramatically amplifying signals for ultrasensitive spectroscopies such as surface-enhanced Raman spectroscopy (SERS).

Beyond plasmonic NPs, gold nanoclusters (AuNCs) exhibit unique fluorescence properties due to their molecular-like electronic structures.[14,15] Their size-dependent emission, high photostability, and biocompatibility make them ideal for bioimaging, biosensing, and drug delivery. Protein-stabilized AuNCs further enable targeted imaging and therapy, with their ultrasmall size (<2 nm) facilitating renal clearance and minimizing long-term toxicity. Additionally, their role as fluorescence contrast agents and reactive oxygen species (ROS) modulators broadens their potential in cancer diagnostics and redox-based therapies.[16]

This review presents recent developments in noble metal-based nanomaterials (**Figure 1**), highlighting their potential to revolutionize biomedical applications through precise optical tuning, enhanced imaging capabilities, and innovative therapeutic strategies.

2. Gold Nanoparticles for Theragnostic

AuNPs exhibit unique and tunable optical properties, primarily due to their LSPR, making them highly attractive for theragnostic (diagnostic imaging and therapeutic interventions) applications (**Figure 2A**).[17] These properties can be precisely controlled by manipulating the particles' shape and size, surface chemistry, and functionalization strategies. In this section, we first examine how different morphologies influence their optical and biomedical properties. We then discuss the role of ligands in stabilizing AuNPs and modulating their behavior in biological environments. Finally, we explore how these optimized properties are being leveraged in plasmonic-based NMs for diagnostic and therapeutic use. By integrating these aspects, we aim to present a coherent framework for the design and application of AuNPs in next-generation theragnostic systems.

2.1. Morphologies of Gold Nanoparticles and Their Biomedical Relevance

AuNPs can be broadly classified as isotropic (spherical, e.g., spheres) or anisotropic (non-spherical, e.g., rods, stars, shells) based on their morphologies, which significantly impacts their interaction with light and, in turn, their biomedical applicability (Figure 2B).[18] Isotropic particles typically absorb in the visible range (520–540 nm),[19] while anisotropic shapes shift their LSPR peaks into the infrared (IR) region, enhancing safety penetration in biological tissues.[20] For example, gold nanorods can be tuned by altering the length of their *Y*-axis, which modifies their interaction with light and shifts their LSPR into the biological window.[8] Gold nanoshells exhibit similar tunability by adjusting their core-to-shell dimensions (Figure 2C). Other shapes, such as gold nanostars, can also tune their LSPR from 600 to

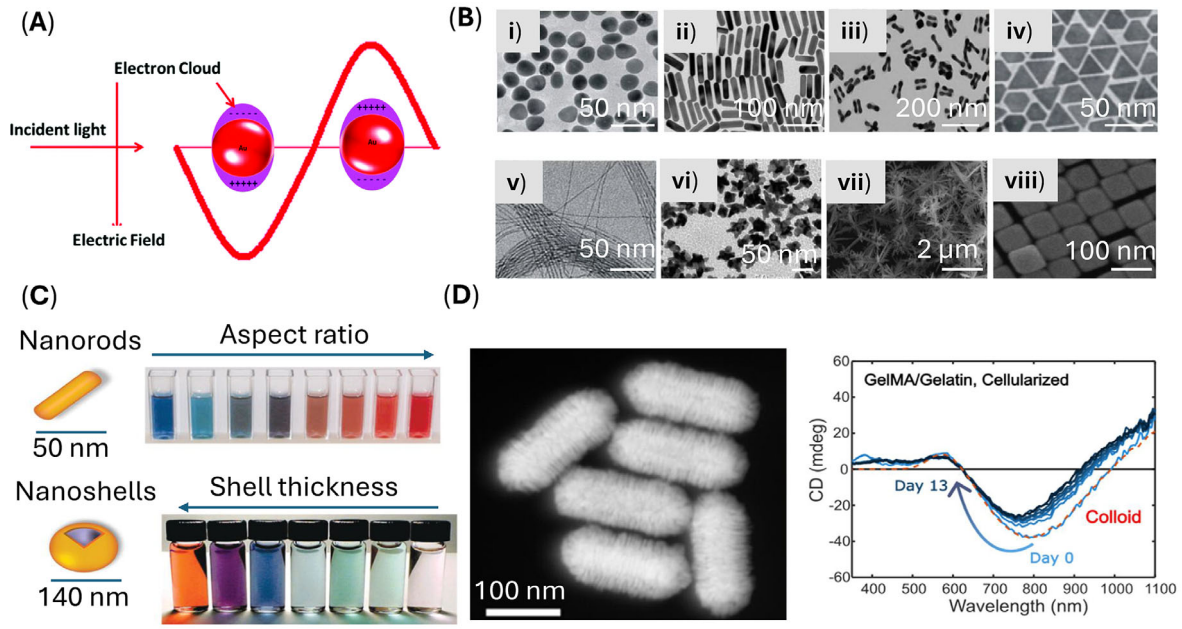

Figure 2. AuNPs properties and physical aspects. A) Scheme of the localized surface plasmon resonance (LSPR). Reproduced or adapted under the terms of the CC-BY 3.0 license ref.[35] Copyright 2020 the Royal Society of Chemistry. B) Transmission Electron Microscopy (TEM) images displaying several morphologies: (*i*) Au nanospheres. (*ii*) Au nanorods. (*iii*) Au nanodumbbells. (*iv*) Au nanoprism. (*v*) Au nanowires. (*vi*) Au nanostars. (vii) Au nanodendrites. (viii) Au nanocubes. Reproduced or adapted with permission from ref.[8] Copyright 2018 Elsevier. C) Optical aspect showing the color change of Au nanorods and Au nanoshells in the axial axis and shell thickness function, respectively. Reproduced or adapted with permission from ref.[8] Copyright 2018 Elsevier. D) High-angle annular dark field scanning transmission electron microscopy (SEM) of chiral gold nanorods and circular dichroism (CD) spectra of a GelMA/Gelatin nanocomposite scaffold with breast cancer cells taken at regular time intervals. Reproduced or adapted with permission from ref.[27] Copyright 2025 American Chemical Society.

1200 nm by adjusting the concentration of Ag^+ ions during synthesis, which influences both the number and length of the spikes.[21]

This easy optical tunability directly impacts biomedical applications (**Table 1**). For example, Rahimi et al. improved the performance of an *Escherichia coli* (*E. coli*) detector by incorporating gold nanospheres onto the surface of a nanobiosensor.[22] This enhancement significantly increased the current conductivity due to the exceptional electrical capabilities of AuNPs, enabling the system to detect analytes at lower concentrations. Similarly, in a Bovine Serum Albumin (BSA) detector, spherical gold NPs were incorporated to enhance sensitivity after the BSA antigen–antibody interaction.[23] This improvement was achieved through plasma hybridization with LSPR. Ziaul Hyder et al. utilized similar spherical particles to enhance the detection and quantification of ciprofloxacin levels in the environment.[24] In sensing, this type of NPs has also been applied to enhance Raman scattering, enabling the visualization of 3D pancreatic tumor models and pushing the boundaries of resolution.[25] While the cited examples demonstrate the use of AuNPs in diagnostic applications, spherical-shaped materials have also shown potential in therapeutic contexts. For instance, Noh et al. developed a contact lens for ocular cystinosis.[26] The binding interaction between cystinosis and the AuNPs enabled monitoring of cystinosis concentration through a color change (diagnosis) while simultaneously serving as a treatment. The concentration of cystinosis was reduced as it spontaneously bound to the AuNPs within the lens, observing ≈9 µg cystine removed from a 50 µM initial concentration.

Thanks to the bathochromic plasmonic band shift of anisotropic AuNPs to the biological window area (NIR), advanced theragnostic applications have been reported. Liz-Marzán et al. recently demonstrated the use of chiral gold nanorods for monitoring local extracellular environments (Figure 2D).[27] They incorporated chiral gold nanorods into GelMA hydrogel nanocomposite scaffolds, a material commonly employed in 3D cell culture. By leveraging circular dichroism (CD), they successfully detected changes in the refractive index, which were directly correlated with the activity of invasive cancer cells. Similarly, gold nanorods have been utilized by the same group as theragnostic agents, demonstrating excellent PTT capabilities in both 2D and 3D tumoral cultures.[28] Additionally, an ^{18}F radioisotope was incorporated to enable visualization of material accumulation in the tumoral area using positron emission tomography (PET).

Gold nanostars are among the most well-known anisotropic AuNPs for therapeutic applications. Zhuang et al. developed core–shell gold nanostars to enhance the thermodynamic stability of AuNPs while serving as effective photothermal agents.[29] By utilizing laser irradiation within the first biological window (808 nm), their system successfully achieved complete ablation of 4T1 tumors in a mouse model over a 20-day experiment, demonstrating excellent therapeutic efficacy. In sensing applications, this shape enhances SERS spectroscopy.[30] Due to their ability to undergo cellular endocytosis, they can label a wide variety of

Table 1. Summary of gold nanoparticle (AuNPs) shapes and their biomedical applications.

Gold nanoparticle shape	Biomedical application	How does it work?	Refs.
Sphere	*Escherichia coli* detector	Excellent current conductive of AuNPs enables analyte detection at low concentration	[22]
	Bovine Serum Albumin detector	BSA antigen–antibody plasma hybridization with LSPR from AuNPs enhances BSA detection sensitivity	[23]
	Visualization of 3D pancreatic tumor models	Raman scattering enhanced via AuNPs	[25]
	Contact lenses for ocular cystinosis	Cystine binds to AuNPs changing the color for monitoring (diagnosis) and reducing their presence in the eye (treatment)	[26]
Rods	Monitoring local extracellular environments	Chiral rods incorporated into GelMa hydrogel scaffolds. Via circular dichroism detection of activity of invasive cancer cells.	[27]
	2D and 3D tumoral cultures ablation	Photothermal capabilities via converting an infrared laser into heat	[28]
Stars	4T1 tumor ablation in a mouse model	Core–shell stars with enhanced thermodynamic stability for photothermal therapy	[29]
	Improved cell imaging	SERS spectroscopy	[30,31]
Nanodumbbells	Cardiac troponin I aptasensor in human blood samples	Immobilize an aptamer with the AuNPs to enhance troponin detection	[32]
Nanocages	Cell imaging	Highest photoluminescence quantum yield in comparison with other shapes	[33]
Nanodendrites	Nucleic acid detection	Plasmon-enhanced electrochemiluminescence with selective biomolecules detection	[34]

Table 2. Summary of some ligands and their main applications for AuNPs.

Ligand	Application	Refs.
Polyvinylpyrrolidone with varying impurities	Fine-tune the formation of the spike in a gold nanostar	[40]
Ultrathin chemically cross-linked nanogels of pAcrylamide or pNIPAM	High stability of gold nanostars and nanorods during prolonged laser irradiation (PPT)	[38]
Carboxylic-PEG	Tumor accumulation of gold nanorods	[28]
	Protein corona adhesion, favorable electrostatic interactions and hydrogen bonding	[43]
Dihydrolipoic acid	Nonspecific protein adsorption reduces the protein corona effect	[44]
Citraconic amide	Gold nanospheres aggregate inside the cell due to a pH change toward acidic, unlocking PPT in the infrared	[45]
DNA-ligand	Thermoresponsive DNA hybridization with AuNPs, inducing reversible aggregation	[46]
Furin enzyme	Intracellular aggregation of AuNPs, seven-fold in vivo tumor reduction via PPT after 18 days	[48]
Elastin	AuNPs aggregation to enhance particle visualization via photoacoustic or X-ray computed tomography	[49]
Diarizine-PEG		[50]
RGD peptide	Cytoplasmic accumulation of AuNPs by binding to $\alpha v\beta 6$ integrins on the cell surface	[55]
MLS peptide	AuNPs target mitochondria	
NLS peptide	AuNPs target the cellular nucleus	
PEI	Accumulation of AuNPs in cytoplasmic organelles (endosomes, lysosomes, lipid droplets)	[56]
dPGS		
AS1411 aptamer	Target the nucleolin receptor overexpress on breast cancer cells	[58]
Membrane proteins from *Shewanella oneidensis* MR-1	Disrupt tumor cell redox balance via an electron transfer mechanism, producing cell death	[59]
Ramucirumab	Enhance cellular uptake in advanced gastric cancer	[60]
Cyclodextrin-Adamantane host–guest	Enhance tumor targeting with low nonspecific liver accumulation and improve treatment via chemotherapy combined with PTT	[61]

cells, enabling improved imaging over extended periods.[31] Furthermore, they allow the identification of cellular traces over time with high precision.

To date, various shapes of AuNPs have demonstrated a wide range of applications. For example, gold nanodumbbells have been used to immobilize an aptamer for the development of a Cardiac troponin I (TnI) aptasensor.[32] This sensor exhibits an impressive limit of detection (LOD) (8 pg mL^{-1}) and successfully diagnosed 85% of blood samples from a cohort of 89 individuals. Gold nanocages demonstrate fluorescence for cell imaging due to their ability to achieve the highest photoluminescence quantum yield (PLQY) among all AuNPs.[33] Additionally, they enable PTT for cancer cells, offering dual functionality in biomedicine. Similarly, gold nanodendrites serve as plasmon-enhanced electrochemiluminescence platforms for nucleic acid detection.[34] Their highly porous structure enables the selective detection of diverse biomolecules with high sensitivity.

While the shape of AuNPs determines their intrinsic optical and electrical properties, their behavior in complex biological environments—and their long-term functionality—depends largely on the surface ligands used for stabilization and functionalization. In the following section, we examine how these ligands influence nanoparticle performance and enable stimulus-responsive behaviors for theragnostic applications.

2.2. Ligands Used for the Stabilization of Gold Nanoparticles

Surface ligands are critical for stabilizing AuNPs and tuning their physicochemical interactions with biointerfaces (**Table 2**), such as salts, proteins, and cellular membranes, and heat generated during PPT applications, thereby directly influencing their long-term stability.[36–39] Traditional ligands such as polyvinylpyrrolidone (PVP) and citrate remain widely used. However, a recent study by Liz-Marzán et al. demonstrated that impurity profiles in PVP can fine-tune anisotropic features such as nanostar spike formation.[40] Their findings revealed that, in the absence of impurities, spherical NPs are produced, whereas the specific base and impurities generated during the polymerization of PVP with hydrogen peroxide play a crucial role in inducing anisotropy. These results have paved the way for "à la carte" gold nanostars through ligand modulation. Besides, other works have employed organic or inorganic shells, biomolecules, and metal coatings to provide advanced protection (**Figure 3A**).[36]

To prevent shape distortion during PPT, when AuNPs typically aggregate,[41] ligand design has evolved from PEG coatings to advanced materials such as chemically cross-linked ultrathin nanogels, based on pAcrylamide or poly(N-isopropylacrylamide) (pNIPAM), that dynamically conform to the rods and stars' gold core morphology and resist laser-induced aggregation (Figure 3B).[38] However, the proper visualization of these organic ligands remains challenging due to their low contrast compared to AuNPs. One of the most recent solutions is the use of high-quality graphene liquid cells.[42] They allow for improved visualization of the ligand distribution in liquid environments compared to traditional carbon-based transmission electron microscopy (TEM)–dried grids (Figure 3C).

Ligands also influence biodistribution and targeting efficiency. For instance, PEGylated gold nanorods with terminal carboxylic groups showed enhanced tumor accumulation compared to those with amines.[28] The authors of this study hypothesize that this phenomenon is produced due to reduced liver uptake, which increases bioavailability shortly after administration. To track them into the tumors, the authors radiolabeled the AuNPs with ^{19}F, thanks to the great affinity between gold and ^{19}F, and monitored their distribution using PET.

When using AuNPs for biomedical applications, the formation of a protein corona (PC) due to uncontrolled protein adsorption remains a major challenge. Antifouling ligands, like PEG, have typically been used to minimize particle–protein interactions. Studies have shown that AuNP's morphology and surface-ligand chemistry act in concert to govern PC formation. High-curvature architectures, such as star- and cage-shaped AuNPs exhibit greater surface area and binding sites, leading to enhanced protein adsorption compared with spherical or rod-shaped counterparts.[43] When these particles are coated with PEG chains terminating in different functional groups (carboxyl, amine, or methyl), carboxyl-terminated PEG yields the strongest corona formation, likely driven by favorable electrostatic interactions and hydrogen bonding. Moreover, the ligand size significantly influences PC formation. Small ligands, such as dihydrolipoic acid (DHLA) or citrate, promote nonspecific protein adsorption on spherical AuNPs.[44] However, modifying DHLA with PEG blocks or zwitterionic groups eliminates these interactions, enhancing AuNPs stability in protein-rich environments. Together, these insights highlight how precise control over particle geometry and ligand functionality can be leveraged to tune stealth characteristics or promote selective biological interactions in theragnostic applications.

For biomedical applications, AuNPs are exposed to diverse physiological environments that vary in temperature, pH, and redox potential. To enhance their performance and functionality under these dynamic conditions, smart ligands, also known as stimuli-responsive ligands, have been employed to endow AuNPs with environment-sensitive intelligence. Selecting the appropriate smart ligand enables selective particle aggregation. For instance, using citraconic amide as a ligand for gold nanospheres induces aggregation only inside the cell due to a shift toward acidic pH.[45] This triggers a bathochromic plasmonic shift, unlocking PTT capabilities in the infrared region. Likewise, DNA-coated AuNPs enable thermoresponsive DNA hybridization among particles, inducing reversible aggregation and shifting the plasmonic band to the infrared region with potential PTT applications (Figure 3D).[46] Similarly, spherical nucleic acids with gold nanospheres at their core have been shown to produce identical effects.[47] Indeed, this capability of converting infrared light into heat is particularly crucial for cancer treatments. Beyond enabling intelligent particle aggregation, ligands must also ensure efficient cellular uptake of AuNPs and prolonged tumor accumulation. To this end, enzymes like Furin—a trans-Golgi protein convertase upregulated in various tumors—have been explored as AuNP ligands.[48] By inducing intracellular aggregation, Furin-coated AuNPs achieved a seven-fold reduction in mouse tumor volume via photothermal ablation after 18 days, compared to control particles without enzyme-induced aggregation.

Beyond treatment, smart ligands also facilitate multimodal imaging. Thermoresponsive polymers such as elastin,[49] or light-sensitive ones like Diazirine-PEG,[50] enhance visualization in

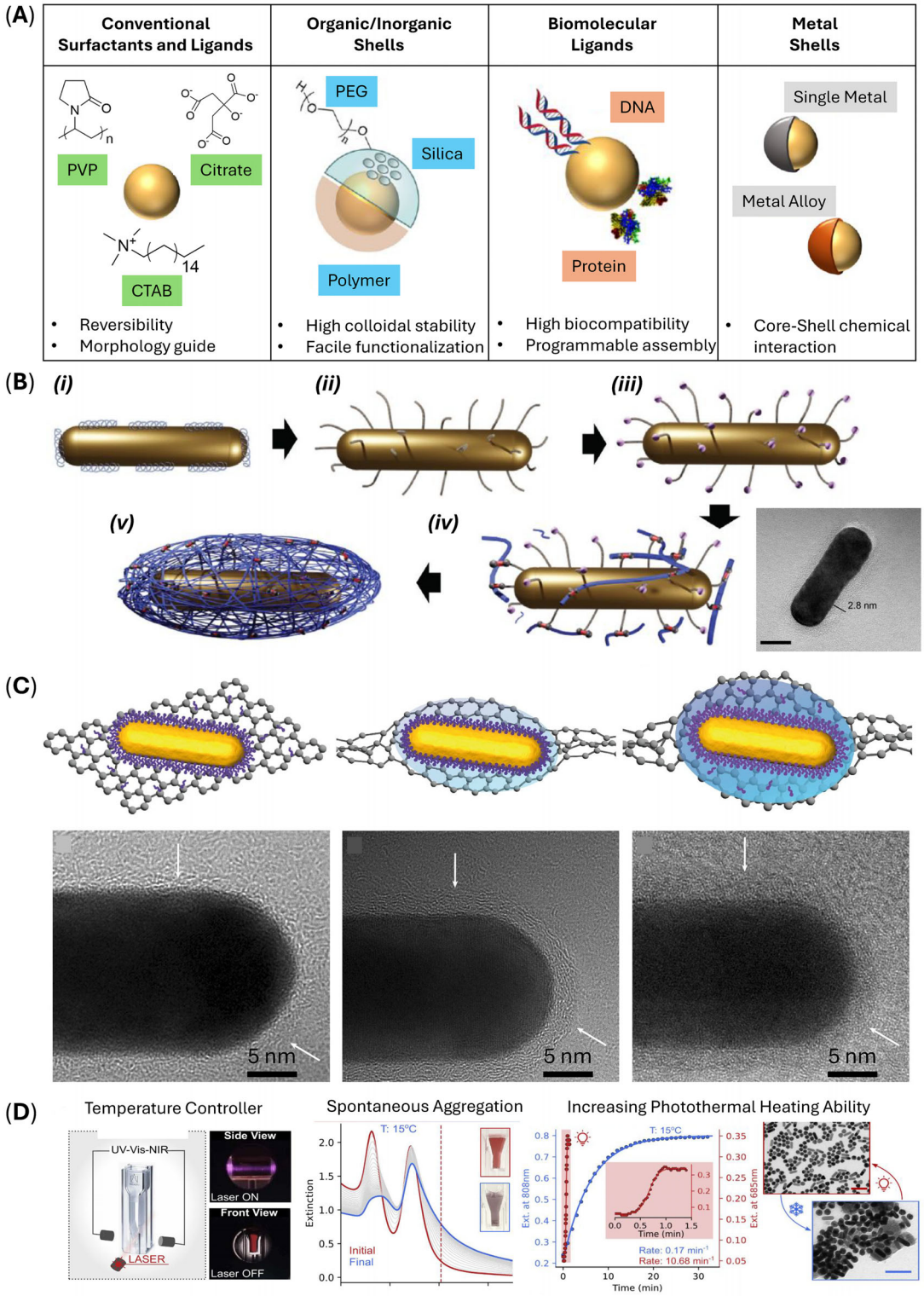

Figure 3. Ligands used for the stabilization and protection of AuNPs. A) Scheme of the most used stabilization strategies for colloidal Au NPs, such as surfactants, ligands, organic and metallic shells, or biomolecular ligands. Reproduced or adapted with permission from ref.[36] Copyright 2019 American Chemical Society. B) Ultrathin chemically crosslinked anisotropic nanogels enhance the stability of rod- and star-shaped AuNPs during prolonged laser irradiation while preserving their optical properties. Reproduced or adapted under the terms of the CC BY-NC 4.0 license, ref.[38] Copyright 2024 John Wiley & Sons, Inc. C) Direct visualization of ligand around gold nanorod observed by TEM in a dried state on a graphene grid and a liquid environment. Reproduced or adapted with permission from ref.[42] Copyright 2024 Springer Nature. D) Assembly/aggregation of AuNPs induced by reversible DNA hybridization enables a bathochromic plasmonic shift, unlocking PTT capabilities in the NIR region. Reproduced or adapted under the terms of the CC-By 4.0 license, ref.[46] Copyright 2024 American Chemical Society.

specific scenarios by inducing plasmonic shifts upon aggregation. This shift enables the detection of AuNPs using imaging techniques such as photoacoustic imaging and X-ray computed tomography. This dual functionality makes AuNPs powerful tools for both therapy and diagnostics, with tunable properties that can be precisely controlled by selecting appropriate surface ligands, paving the way for more effective and targeted biomedical applications. Notably, researchers have also begun integrating AuNPs into NMs and micromotors (MMs), further expanding their theragnostic potential.

Ligands also play a crucial role in promoting strong interactions with biological systems.[51,52] AuNPs with specific cancer-target ligands can easily internalize into subcellular organelles and notably reduce cancer cells, acting directly on their nucleus and mitochondria.[53] For instance, once AuNPs are attached to the cell surface, they can enhance phospholipid membrane permeability through mechanisms such as photoporation, in which localized heat generated during PPT induces the formation of nanobubbles around the AuNPs.[54] The expansion and collapse of these nanobubbles disrupt the membrane, producing nanosized pores (**Figure 4A**). Moreover, AuNPs can be targeted not only to the cell membrane but also to specific intracellular compartments such as the cytoplasm, mitochondria, and nucleus.[55] This targeted localization is achieved by functionalizing the AuNPs with specific peptides. For example, the RGD peptide facilitates cytoplasmic accumulation by binding to $\alpha v\beta 6$ integrins on the cell surface. Similarly, the MLS peptide enables mitochondrial targeting, while the NLS peptide directs AuNPs to the nucleus. Such targeted delivery can significantly enhance Raman resonance imaging within these specific cellular regions. The same peptides have also been linked to PEGylated gold nanorods by Xu, et al. to target specific cellular organelles and ablate these localized areas.[56] Polymers such as polyethylenimine (PEI) and dendritic polyglycerol sulfate (dPGS) have also been employed by McNally et al. to functionalize AuNPs, promoting their accumulation in cytoplasmic organelles such as endosomes, lysosomes, and lipid droplets.[57] This targeted localization enhances the visualization capabilities of cryo X-ray tomography (Figure 4B).

For targeted cancer therapies, the conjugation of AuNPs has also proven to be effective. For instance, the aptamer AS1411 has been attached to the surface of AuNPs to specifically target the nucleolin receptor, which is overexpressed on breast cancer cells.[58] Chen-Sheng et al. recently engineered plasmonic liposomes by coating AuNPs with membrane proteins from *Shewanella oneidensis MR-1*, enriching them with c-type cytochromes.[59] This system disrupts the tumor cell redox balance through a unique electron transfer mechanism, triggering lipid peroxidation and mitochondrial dysfunction, ultimately leading to cell death. In mice, this approach significantly reduced tumor size 14 days after treatment (Figure 4C). Besides polymeric ligands, FDA-approved antibodies such as Ramucirumab, used in the treatment of advanced gastric cancer, have recently been conjugated to anisotropic gold nanorods to enhance cellular uptake.[60] In vivo results demonstrated that while tumor cells were effectively targeted and destroyed by the nanodrug, normal gastric cells remained unaffected (Figure 4D). A smart host–guest system developed by Liu et al. utilized AuNPs decorated with the ligand cyclo(Arg-Gly-Asp-D-Phe-Cys) and the host molecule cyclodextrin to specifically target tumors while minimizing nonspecific liver accumulation.[61] A pH-sensitive doxorubicin prodrug, modified with an adamantane group and linked to AuNPs, was designed as the guest component. This guest selectively binds to the host at tumor sites, where the acidic environment triggers drug release. The combination of this chemotherapeutic strategy with PTT led to a significant reduction in tumor size in vivo, approximately a five-fold decrease compared to the control group.

These diverse examples underscore the pivotal role of surface ligands in governing the behavior, stability, and functionality of AuNPs in biomedical settings. From enhancing structural integrity and controlling aggregation to directing cellular uptake and enabling stimuli-responsive behaviors, ligands offer a versatile toolbox for engineering AuNPs with high precision.

2.3. Gold Nanoparticles Used for Plasmonic-Based Nano- and Micro-Motors

MMs and NMs are active particles capable of autonomous motion in biological media, even within highly viscous environments typically found in biological barriers.[62] Their movement can be guided externally using magnetic fields, light, or acoustic signals, or they can self-propel by converting chemical energy into mechanical work through reactions that generate motion-driving byproducts.[63–68] Recently, AuNPs have been chemically bonded or adsorbed onto active materials to enhance motor performance by leveraging the plasmonic properties of gold.

For in vivo imaging, Sánchez et al. functionalized urease-powered, mesoporous-based nanomotors with AuNPs to anchor the ^{124}I radioisotope, enabling their visualization in the mouse bladder via PET.[69] Additionally, the same group utilized the plasmonic properties of AuNPs to achieve high-resolution imaging of nanomotor accumulation in bladder tumors using light-sheet microscopy (**Figure 5A**).[11] This technique, which selectively illuminates a thin focal plane, benefits from AuNPs' excellent dispersibility and strong light absorption, enhancing imaging contrast and resolution.

AuNPs have also enhanced NMs tracking visualization by increasing contrast, paving the way for more advanced imaging techniques. Gold nanospheres anchored to DNA motors enabled high-resolution tracking in reflection interference contrast microscopy (Figure 5B).[70] In similar research, Käll et al. demonstrated that it is also possible to release DNA from gold nanorods, driven by circularly polarized laser light in solution, via photothermal heating, enabling temperature-dependent kinetics and activation energy control.[71]

Liang et al. recently enhanced enzymatic NMs by incorporating gold nanostars, adding PTT capabilities, and SERS sensing for improved therapeutic efficiency.[72] Cellular studies found that incubating cells with 100 μg mL^{-1} of these plasmonic materials did not affect viability. However, cell viability dropped to 40% when exposed to an NIR laser. This synergistic design improved AuNP internalization due to NMs-driven motion while enhancing laser-induced cellular damage through plasmonic heating. Peng et al. further enhanced the performance of their motors by incorporating gold onto the surface of mesoporous particles (Figure 5C).[73] The gold–silica coupling enabled a controlled plasmonic shift into the IR region. Upon laser irradiation, they observed increased NMs motion due to the self-thermophoretic

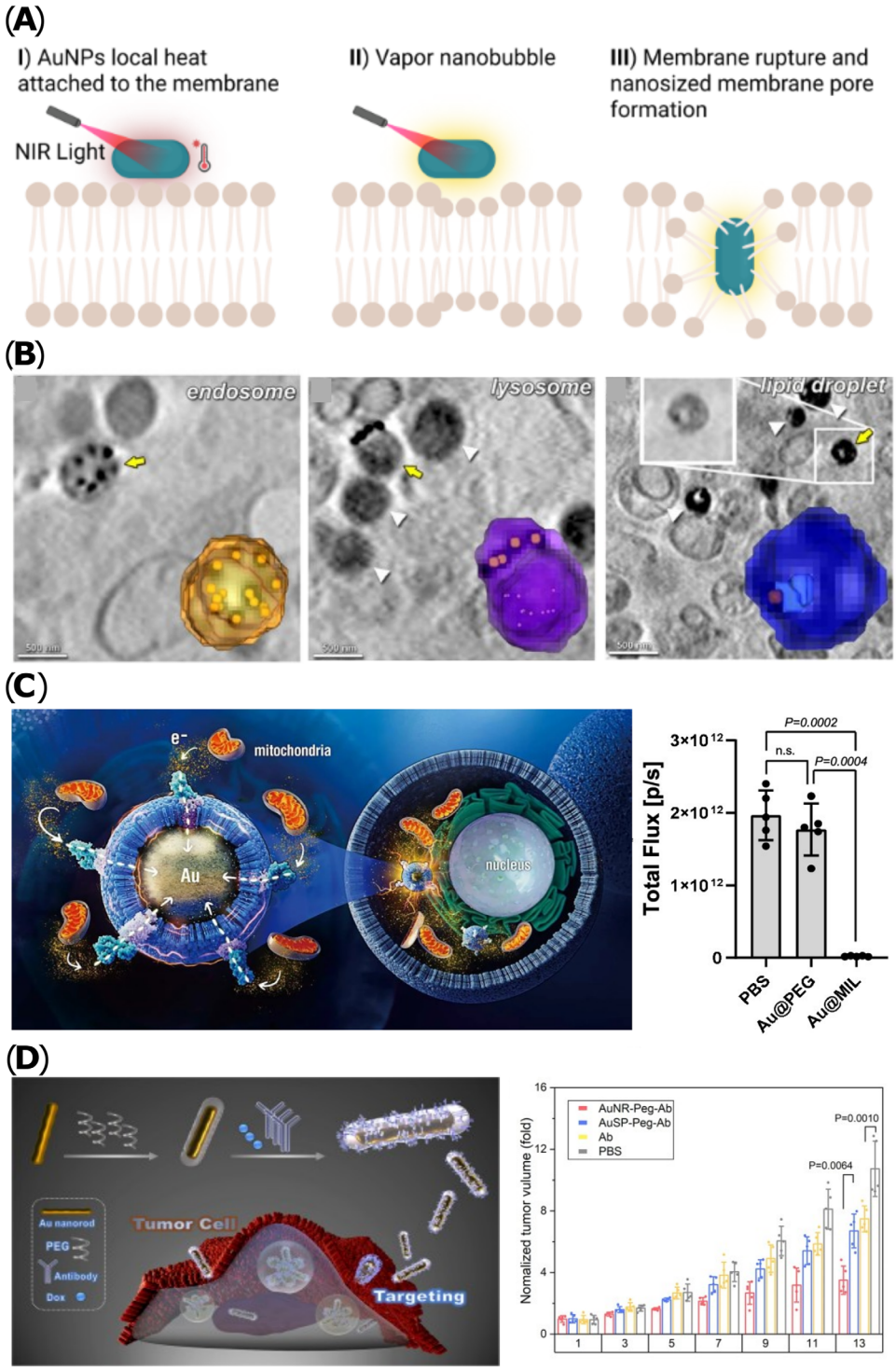

Figure 4. Ligands for targeting specific cells and organelles. A) Photoporation process of gold nanorods. After their binding to the cell membrane, a focused laser causes a temperature increase and nanobubble formation around the rod. Expansion and collapse of the bubbles lead to membrane rupture. Created in BioRender. Sánchez, S. (2025) https://BioRender.com/3vqytqp. B) Endocytic uptake of AuNPs in A549 cells via cryo X-ray tomography, showing localization in the endosome, lysosome, and lipid droplet. Reproduced or adapted with permission from ref.[57] Copyright 2020 American Chemical Society. C) AuNPs covered with electroactive membranes induce cell damage by redirecting electron transfer, disrupting the redox equilibrium within cancer cells. Reproduced or adapted with permission from ref.[59] Copyright 2025 Springer Nature. D) Gold nanorods covered with an antibody for enhanced tumor penetration, resulting in high tumor reduction effects in vivo. Reproduced or adapted under the terms of the CC-BY license from ref.[60] Copyright 2021 Springer Nature.

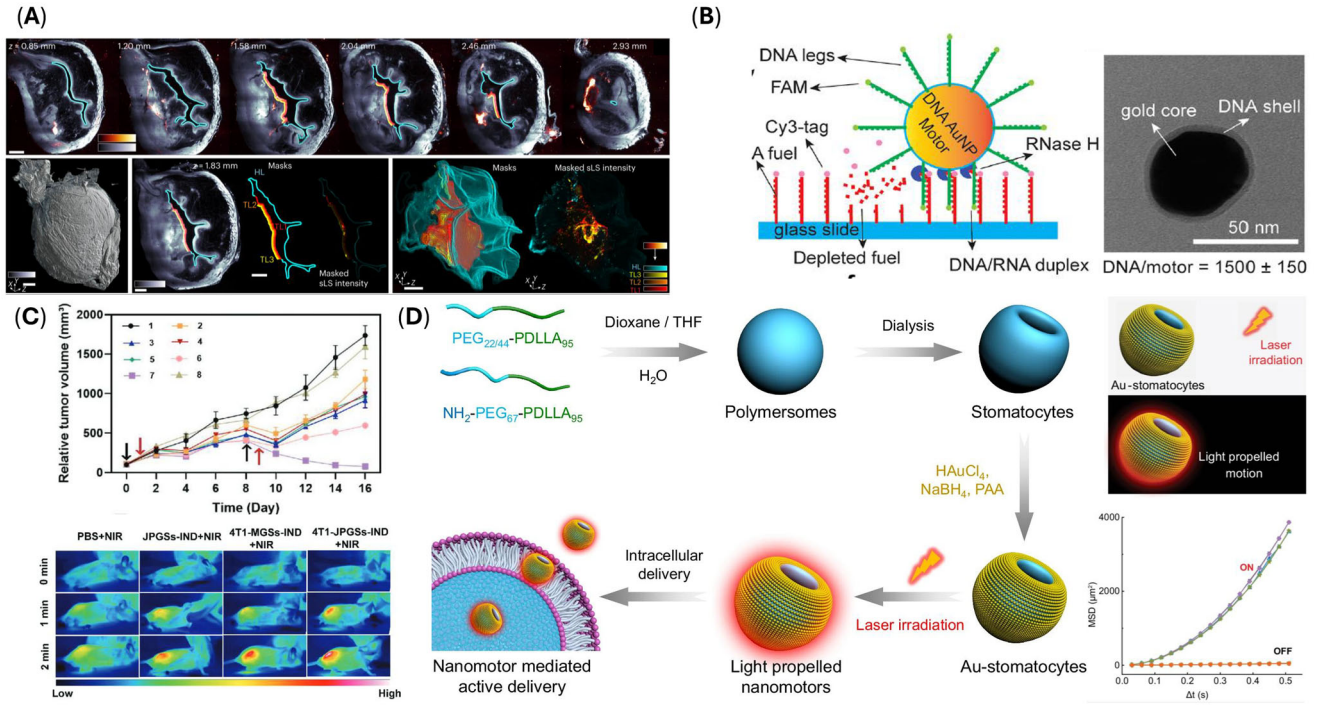

Figure 5. Gold nanoparticles (AuNPs) enhance the photonic properties of nanomotors (NMs). A, left) Light-sheet microscopy images of a mouse bladder showing plasmonic mesoporous NMs accumulated in tumors. (right) TEM microscopy image of gold nanospheres onto the NMs. Reproduced or adapted under the terms of CC-BY license from ref.[11] Copyright 2024 Springer Nature. B) DNA-basedNMs coupled to AuNPs visualized using reflection interference contrast microscopy, showing the trajectories of a single motor. Reproduced or adapted with permission from ref.[70] Copyright 2021 American Chemical Society. C) Relative in vivo tumor volume reduction achieved through the photothermal capabilities of plasmonic-based NMs, along with their localized heat increase in mice. Reproduced or adapted with permission from ref.[73] Copyright 2023 John Wiley and Sons. D) Light-propelled biodegradable stomatocyte NMs with efficient intracellular transport and enhanced mean squared displacement under laser illumination. Reproduced or adapted under the terms of CC-BY license from ref.[74] Copyright 2024 Springer Nature.

effect, driven by thermal flow. This thermo-mechanical percolation facilitated deeper tumor tissue penetration and enhanced tumor cell ablation, which directly correlated with a reduction in tumor volume. Additionally, the heat generated promoted selective tumor accumulation of the motors while mitigating inflammation.

These studies demonstrate that integrating AuNPs into NMs not only enhances imaging resolution and tracking but also improves therapeutic performance through plasmonic heating and targeted activation.

Besides their therapeutic applications, during the light-to-heat conversion process, there is a thermal gradient generated because of the asymmetrically distributed AuNPs that can drive a NM. For instance, Wang et al. depositate AuNPs on biodegradable polymersomes (stomatocytes), yielding light-propelled NMswith exceptional motility (up to 125 μm s^{-1}) in biological media (Figure 5D).[74] The design exploited the nonuniform distribution of AuNPs along the *z*-axis to induce asymmetric plasmonic heating and thus thermophoretic propulsion. A similar strategy is demonstrated in the work from Cao et al., where polymersomes bearing aggregation-induced emission (AIE) moieties were coated with hemispherical Au nanoshells to create phototactic NMs responsive to two-photon NIR irradiation.[75] The synergy between AIE-based fluorescence and AuNP-induced heating enabled both propulsion and reactive oxygen species (ROS) generation for enhanced photodynamic therapy. Likewise, Guo et al. employed Janus MOF@Au NMswhere AuNPs were asymmetrically deposited on MOF particles, enabling NIR-triggered propulsion and improved penetration into dense bacterial biofilms.[76] The Au component not only facilitates active motion but also enhances ROS production under ultrasound through improved electron–hole separation, critical for sonodynamic therapy (SDT). This dual functionalization, locomotion, and enhanced catalysis highlight the versatile role of AuNPs in integrating propulsion with therapeutic action. Chicos et al. used AuNPs agents for thermoplasmonic manipulation to induce thermos-osmotic flows.[77] These flows result from optically generated temperature gradients perturbing van der Waals and electrostatic interactions at the gold–liquid interface, enabling hydrodynamic trapping and manipulation of AuNPs. The study emphasizes emergent hydrodynamic forces as tools for guiding the particles in confined environments, for boundary-driven active matter manipulation. In another work, the same authors outline AuNPs as a source within thermoplasmonic systems for manipulating macromolecules.[78] Here, AuNPs create localized temperature gradients that drive thermophoretic or hydrodynamic flows used to trap or stretch these softer, non-colloidal species. These examples underscore the multifunctionality of AuNPs, where precise thermal control enables not only propulsion and directional manipulation but also synergistic therapeutic effects, positioning them as key enablers in the design of next-generation active and responsive theragnostic technologies.

3. Advances in Plasmonic Nanoparticles for Biosensing and Diagnostics

As mentioned in Section 1, when a small spherical metallic NP is exposed to light at a particular resonance frequency, its conduction electrons are induced to coherently oscillate in a standing-wave-like manner due to the oscillating electric field of the light, referred to as LSPR. The LSPR frequency is influenced by the dielectric properties of the metal and can be tuned within the UV–NIR spectral range by modifying the dimensions of the NP, such as its size and shape, and the surrounding medium. The LSPR excitation can be detected by the extinction spectrum (summed contribution of the far-field absorption and scattering peaks of the LSPR modes) and the near-field intensification around the NPs surface, which is a direct consequence of the resonant electrons. Far-field and near-field properties are explained as two complementary manifestations of LSPR excitation. These optical properties (enhancements of the extinction cross-section and the EM field near the NP surface) have made plasmonic NPs a widely used tool in biosensing, imaging, and therapeutic applications.[79]

This section will further discuss biosensing applications of plasmonic NPs by addressing their so-called far-field and near-field optical properties, and how they have become a game-changer in modern biomedical research and clinical diagnostics. Integrating their ability to provide enhanced optical contrast, unparalleled sensitivity, and specificity in detecting and quantifying biomolecular interactions makes them promising candidates for a wide range of biomedical applications, from biospectroscopy to targeted cancer therapies.[80,81]

3.1. Far-Field Properties

Far-field interactions are related to the scattering and absorption properties of NPs when exposed to light, leading to measurable changes in their extinction spectra. These optical responses play a critical role in biosensing and imaging applications, where precise spectral shifts can be leveraged for molecular detection and contrast enhancement.[81–83] The far-field response of NPs is highly dependent on key parameters such as their size, shape, and the refractive index of the surrounding medium, which collectively influence their optical cross-sections and plasmon resonance characteristics.[84]

The extinction cross-section (C_{ext}) is the sum of the absorption (C_{abs}) and scattering (C_{sca}) cross-sections, expressed as:

$$C_{ext} = C_{abs} + C_{sca} \tag{1}$$

These quantities are governed by the polarizability (α) of the NP. In the quasi-static approximation—valid for particles much smaller than the incident wavelength—the polarizability of a spherical particle embedded in a non-absorbing medium with dielectric constant ϵ_n is given by:

$$\alpha = 4\pi a^3 \left[\left(\varepsilon(\omega) - \varepsilon_0 \right) / \left(\varepsilon(\omega) + 2\varepsilon_0 \right) \right] \tag{2}$$

where a is the particle radius, and $\epsilon(\omega)$ is the frequency-dependent complex dielectric function of the nanomaterial.[85,86]

This expression shows that the polarizability—and consequently the far-field optical response—is directly determined by the nanoparticle composition, as it defines $\epsilon(\omega)$. For instance, silver exhibits a lower imaginary component of $\epsilon(\omega)$ than gold in the visible range, resulting in sharper and more intense scattering resonances. This explains the enhancement in detection performance when coating AuNPs with silver shells, as discussed in later sections.

For anisotropic particles such as spheroids, the polarizability depends on shape through a shape factor Xj. The polarizability along axis j is given by:[6]

$$\alpha \mathrm{j} = \mathrm{V} \left[\left(\varepsilon(\omega) - \varepsilon_0 \right) / \left(\varepsilon(\omega) + \mathrm{Xj}\varepsilon_0 \right) \right] \tag{3}$$

Here, V is the NP volume, and $Xj = 1/Lj$, with Lj being the shape-dependent depolarization factor along axis j. In the case of nanorods, increasing the aspect ratio shifts the localized surface plasmon resonance (LSPR) peak into the near-infrared region and enhances light–matter interactions. Thus, shape modulation provides a powerful strategy for engineering the plasmonic response.

From the polarizability, the optical cross-sections are obtained as:

$$\mathrm{Cabs} = 4\pi \mathrm{k}\ \mathrm{Im}(\alpha) \tag{4}$$

$$\mathrm{Csca} = (8\pi/3)\,\mathrm{k}^4 |\alpha|^2 \tag{5}$$

$$\mathrm{Cext} = \mathrm{Cabs} + \mathrm{Csca} \tag{6}$$

where $\mathrm{k} = 2\pi \mathrm{n}/\lambda$ is the wavevector in the embedding medium with refractive index n. These equations emphasize how structural (size, shape) and compositional (material dielectric function) factors jointly control the absorption and scattering behavior of plasmonic nanostructures.[6,85]

Later in the review, we discuss how compositional modifications, such as the use of AgNPs or the growth of Ag shells around Au cores (Au@Ag), improve detection capabilities by increasing scattering efficiency and EM enhancement. For example, we demonstrate how silver shell growth enhances both far-field (e.g., in IDILA) and near-field (e.g., in label-free SERS detection of exosomes) responses, leading to superior sensitivity and specificity.

These theoretical insights and experimental validations illustrate how precise engineering of NP composition and morphology enables tuning of their optical properties for advanced biosensing applications.

Experts in the field have exploited their understanding of how parameters such as particle size, aggregation state, and interparticle distance, which affect the plasmon coupling effect, have developed far-field-based nanobiosensors. One of the clear examples is plasmonic enzyme-linked immunosorbent assay (pELISA), which combines the working principle of LSPR with that of traditional ELISA to develop a visually detectable signal to biomolecular interaction, for example, antigen-antibody binding. In conventional sandwich ELISA, the target molecule is anchored to the substrate by capturing antibodies and recognized by primary antibodies. The last ones are coupled to enzymes whose biocatalysis generates a colored compound (**Figure 6**A). In pELISA, the biocatalytic reactions used in this assay trigger changes in

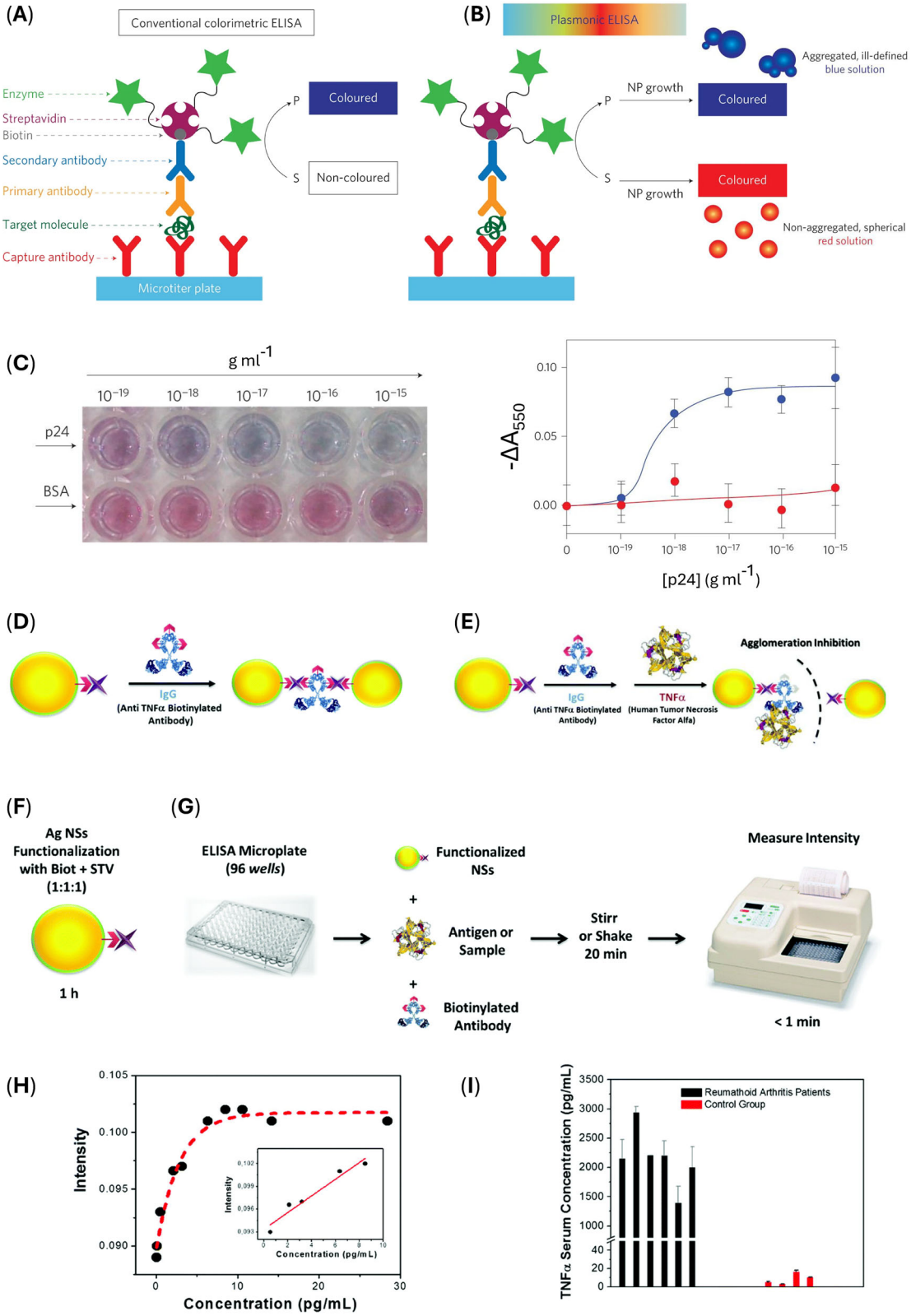

NP size, shape, or aggregation, directly modulating their LSPR behavior.[87] Changes in the state of aggregation, size, or shape of NPs result in shifts in the LSPR wavelength, which can be observed as color changes. In some pELISA setups, the presence of a target analyte induces enzymatic reactions that alter the charge or surface chemistry of NPs, leading to their aggregation, reducing particle distance and causing a coupling of their plasmonic fields. This results in a red shift in the LSPR peak and a visible color change, such as from red to blue (Figure 6B). Enzymes like catalase or alkaline phosphatase catalyze reactions that produce reducing agents (e.g., hydrogen peroxide or ascorbic acid), which reduce metal ions to form NPs. The presence of analytes controls the growth kinetics of these particles, determining their size and morphology. Smaller, spherical NPs typically exhibit a red color, while larger or irregularly shaped aggregates appear blue. In some strategies, enzymes mediate reactions that deposit additional metal layers on existing materials, increasing their size and shifting their LSPR peaks.[88] Alternatively, enzymes may catalyze the etching of NPs, modifying their shape and causing distinct color changes, thus leveraging the optical properties of metal NPs to provide an ultrasensitive and visually intuitive diagnostic platform.[89]

The pELISA concept was first introduced by the foundational work by de la Rica and Stevens, in which they demonstrated the use of enzyme-controlled gold NP growth to generate color changes (Figure 6C).[90] This approach, based on the modulation of hydrogen peroxide levels, led to the formation of either red (non-aggregated NPs) or blue (aggregated NPs), providing an intuitive diagnostic signal that enabled the detection of biomarkers like prostate-specific antigen (PSA) and HIV-1 capsid antigen p24 at attomolar concentrations, achieving unprecedented levels of sensitivity (**Figure** 6C).[90] Xuan et al. further elaborated on similar techniques involving silver NPs, highlighting their high extinction coefficients and versatility in diagnostics.[91]

Conventional enzyme-linked immunosorbent assay (ELISA) relies on enzymatic biocatalysis to develop a colorimetric signal, which would be proportional to the concentration of the analyte. However, the sensitivity of this method is limited by the weak absorption coefficient of organic dyes commonly used as chromogenic substrates (e.g., tetramethylbenzidine, TMB) that renders a LOD at nanomolar ranges ($\approx 10^{-9}$ M) for most biomarkers and sensitivity often proves to be insufficient for low-abundance biomarkers, particularly in early stages of disease.[93] On contrast, pELISA can significantly enhance the sensitivity due to the enhanced extinction coefficient of noble metal NPs that can be orders of magnitude larger than organic dyes, and since color changes are produced through LSPR modulation, these are visually detectable even at ultralow analyte concentrations (attomolar range $\approx 10^{-18}$ M). For example, de la Rica and Stevens demonstrated LODs as low as 10^{-18} g mL^{-1} for prostate-specific antigen (PSA) and HIV-1 capsid antigen p24 using gold NP growth mechanisms.[90] Other studies have achieved LODs in the femtomolar range ($\approx 10^{-15}$ M) for biomarkers like alpha-fetoprotein (AFP) and IgG antibodies by controlled growth of silver NPs.[91]

Another interesting approach for exploiting the optical properties of plasmonic NPs relies on the controlled aggregation through the so-called Intensity Depletion Immuno-Linked Assay (IDILA).[92] IDILA is an enzyme-free immunoassay designed to overcome the limitations of conventional ELISA, such as enzymatic instability, nonspecific binding, and the need for multiple washing steps. IDILA operates on the principle of silver NP (AgNP) dimerization controlled by antigen–antibody interactions (Figure 6D). The formation of AgNP dimers results in distinct optical signals due to changes in LSPR, which are used to quantify analyte concentrations. In the presence of a target antigen, dimer formation is inhibited, leading to depletion in the optical extinction signal (Figure 6E). This extinction changes form the basis of analyte detection and has been demonstrated to allow femtomolar sensitivity under optimized conditions, as shown by Mercadal et al. using AuNPs as a plasmonic substrate.[94] As no enzymatic steps are needed, it has a faster execution (≈2 h) and lower reagent consumption, while keeping an exceptional sensitivity (Figure 6F,G). Moreover, by optimizing NP size and dimerization conditions, IDILA achieves detection limits of several orders of magnitude lower than conventional ELISA, as shown in Figure 6H. This technique was able to diagnose antigens in clinical serum samples from rheumatoid arthritis patients (Figure 6I).

IDILA and plasmonic ELISA represent significant advancements in biosensing, utilizing LSPR to enhance detection sensitivity beyond the limits of conventional ELISA. While plasmonic ELISA offers exceptional sensitivity for ultra-trace analyte detection, IDILA stands out for its enzyme-free design, robustness, and ease of implementation. The future of these plasmonic techniques lies in their integration with advanced technologies involving microfluidics, digital analysis, and artificial intelligence (AI) to enhance multiplexing capabilities and real-time monitoring. Together, these technologies highlight the potential of nanoplasmonics in revolutionizing diagnostic platforms.

The far-field optical properties of plasmonic surfaces, whether through direct metal deposition or nanostructure integration,

Figure 6. High-Sensitivity Immunoassay Strategies: Plasmonic ELISA (pELISA) and Intensity Depletion Immuno-Linked Assay (IDILA). A) Scheme of conventional sandwich ELISA: the target molecule is anchored to the substrate by capturing antibodies and recognized by primary antibodies. The last ones are cupped to enzymes whose biocatalysis generates a colored compound. B) Scheme of plasmonic ELISA, in which the biocatalytic cycle of the enzyme generates colored nanoparticle solutions of characteristic tonality (S, substrate; P, product; NP, nanoparticle). C) Detection of HIV-1 capsid antigen p24 by the generation of blue NP solutions. The signal ($-\Delta$A550) is expressed as the decrease in absorbance concerning the blank monitored at 550 nm. Blue curves were obtained by spiking p24 in female serum. Red curves were obtained by spiking the unrelated protein BSA. Error bars indicate the standard deviation of three independent measurements. Reproduced or adapted with permission from ref.[90] Copyright 2012 Springer Nature. D) Schematic representation of the NP functionalization strategy and E) schematic representation of the IDILA assay procedure: The functionalized NPs are added to the ELISA microplate of 96 wells together with the specific biotinylated antibody (Biot-IgG), and the recombinant antigen or the real sample. F) Schematic representation of the NP-controlled agglomeration strategy (dimer formation) in the presence of a biotinylated antibody (Biot-IgG). G) Schematic representation of the dimer formation avoided in the presence of the specific antigen (TNFα). H) Calibration curve of the antigen using biotinylated anti-human TNFα and recombinant human TNFα. I) Quantification of antigen in real clinical samples using serum from rheumatoid arthritis patients and serum of healthy control subjects. Reproduced or adapted with permission from ref.[92] Copyright 2016 The Royal Society of Chemistry.

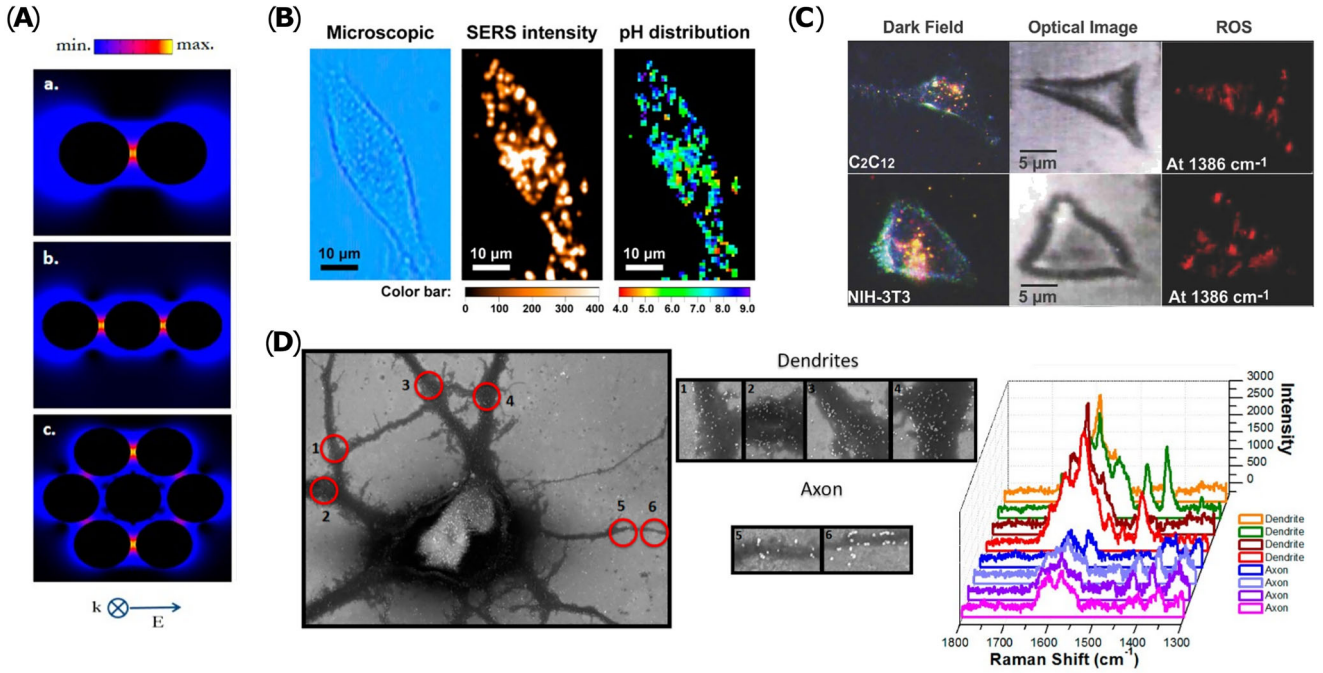

Figure 7. Near-Field Plasmonic Effects: EM-Field Enhancement and Their Role in Biosensing. A) Spatial distribution of EM-field enhancement at 488 for 56 nm Ag sphere compact nanocluster configurations (interparticle distance = 5 nm). Reproduced or adapted with permission from ref.[104] Copyright 2013 American Chemical Society. B) AMB-Tat fluorescent probe for the intracellular pH imaging of a single living CaSki (human cervical carcinoma) cell: Microscopic image was observed under the bright-field illumination; SERS intensity image was produced by using the intensities of 1093 cm^{-1} peak; pH distribution image was produced by correlating the intensity ratio of 1208 to 1274 cm^{-1} peaks with pH values. Reproduced or adapted with permission from ref.[105] Copyright 2019 American Chemical Society. C) ROS imaging of live cells using SERS nanoprobes: dark-field image, bright-field image, and Raman mapping image corresponding to the band at 1386 cm^{-1} for ROS measurements. Reproduced or adapted with permission from ref.[106] Copyright 2017 John Wiley and Sons. D) Quantification of immunolabelled glutamate receptors densities through SERS: Comparative scheme showing the relative intensity changes of the SERS spectra as well as the relative densities obtained in the SEM images associated with the spectral changes in the subcellular protrusions of the neuron cell (dendrites and axon). Reproduced or adapted with permission from ref.[107] Copyright 2014 American Chemical Society.

have been effectively harnessed for label-free biosensing. In that sense, Lechuga et al. have demonstrated how structured plasmonic surfaces enhance light–matter interactions, improving sensitivity for analyte detection. A key example is Blu-ray disc-based nanostructured plasmonic biosensors, which exploit periodic nanoslit arrays to enhance LSPR, achieving sharper resonances and improved detection limits via Fano resonant modes.[95] Their work extends to clinical applications, such as label-free detection of tumor-associated antigens with pM-range sensitivity, surpassing ELISA,[96] and SPR-based biosensors for therapeutic drug monitoring.[97] Additionally, their SPR biosensors have enabled rapid and highly specific COVID-19 serology[98] and real-time detection of pituitary hormones.[99] These advances highlight the potential of far-field plasmonic interactions for ultrasensitive, real-time biosensing in clinical diagnostics.

3.2. Near-Field Properties

Near-field interactions are a complementary manifestation of the LSPR excitation, together with the far-field properties described above, that arise from the strong EM enhancements localized near the NP surface, typically within a few nanometers, and decrease rapidly with distance from the surface, creating a gradient of field enhancement.[85] In NP assemblies, such as dimers or trimers, the interparticle gap significantly amplifies the EM field, forming "hotspots" (**Figure** 7A). These hotspots are regions of intense EM enhancement, and their magnitude and distribution depend on the NP's shape, interparticle distance, and orientation. The interparticle gap plays a critical role in determining the properties of nanostructured materials, as it governs the coupling of LSPR modes between NPs. This coupling can dramatically alter the optical and EM behavior of the assembly, making it a key factor in designing materials with specific plasmonic properties.[100] This has been particularly evident in studies of silver and gold NP dimers, where the optical properties of the system are strongly influenced by the gap between particles.[101–103]

Nanobiosensing exploits the near-field enhancement capabilities of plasmonic substrates, focusing on their near-field properties, through SERS detection. SERS is a plasmonic phenomenon that arises upon the excitation of the plasmon resonance, leading to a substantial enhancement of the electric field surrounding the NP. The dominant mechanism responsible for the SERS effect is widely recognized as EM enhancement. This mechanism is quantified by the EM field enhancement factor (EMFEF), which plays a crucial role in amplifying Raman signals, thereby

improving detection sensitivity in nanobiosensing applications. The EMFEF is defined as:

$$EMFEF = |\Gamma(\omega)| \left|\Gamma(\omega')\right| \quad (7)$$

$$|\Gamma(\omega)| = \left(|E(\omega)| / |E_0(\omega)|\right)^2 \quad (8)$$

$$\left|\Gamma(\omega')\right| = \left(\left|E(\omega')\right| / \left|E_0(\omega')\right|\right)^2 \quad (9)$$

where $|\Gamma(\omega)|$ is the ratio of the complex local enhanced EM field at the illumination wavelength (ω) and the incident EM field multiplied by the corresponding complex conjugate, that is, the absolute square of the magnitude of the electric field enhancement and $|\Gamma(\omega\prime)|$ is the square of the enhanced electric field generated at a particular stokes frequency ($\omega\prime$) of the molecule.[104] The SERS Raman intensity (I_{SERS}) can be expressed by an equation that considers specifically the EFEF and the Raman cross-section of the molecule's particular mode excited at the particular wavelength:

$$I_{SERS} = F_s \sigma_s C_{SERS} EMFEF \quad (10)$$

where F_s is an instrumental factor, σ_s is the Raman cross-section of the molecule on the nanostructure, and C_{SERS} is the concentration on the nanostructure.[104]

As previously discussed, the EM field can be further intensified within NP aggregates, particularly in the gap regions between adjacent NPs (hot spots), due to plasmon coupling. This pronounced enhancement enables the strategic design of SERS-based applications, where selecting the appropriate illumination wavelength can facilitate ultrasensitive detection, including the development of bio(nano)sensors. SERS has found extensive applications in various biomedical and cellular research fields due to its exceptional sensitivity and molecular specificity. It has also been widely used for intracellular sensing, monitoring the fluctuation of intracellular pH (Figure 7B),[105,108–110] monitoring intracellular redox potential,[111,112] and imaging reactive oxygen species (ROS) (Figure 7C).[106,113,114] SERS has also been employed to study biomolecular interactions, allowing high-resolution of the distribution of receptors at cell surfaces (Figure 7D).[107,115,116] While these applications continue to forge ahead within biomedical research, one of the up-and-coming areas that is increasingly grabbing scientific attention is the application of SERS to detect exosomes or exosome-like vesicles (ELVs) as biomarkers for cancer prognosis due to their molecular signatures that directly reflect characteristics of their cell of origin.

ELVs are nanosized vesicles, 40–200 nm, circulating in body fluids like blood, urine, and saliva, hence being an ideal candidate for noninvasive liquid biopsies. These ELVs carry along proteins, lipids, RNA, and DNA, which can be used for detection, providing crucial insights into tumor progression, metastasis, and treatment response. Several strategies have been explored to leverage SERS for exosome detection. Wang et al. developed a SERS-based apta-immunoassay using gold shell magnetic nanobeads to capture exosomes via the CD63 protein, followed by SERS probes decorated with Raman reporters and aptamers for multiplex detection of exosomes from various cancers.[117] Stremersch et al. introduced a method to identify individual ELVs using SERS, where exosomes were coated with gold NPs to enhance the Raman signal, enabling differentiation between cancerous and healthy cell-derived vesicles even in mixed populations.[118] Other materials have been explored to develop cost-effective SERS substrates. For example, Li et al. explored a novel nanostructured platinum-black (Pt-black) SERS substrate for detecting breast cancer-derived exosomes, able to differentiate exosomes from triple-negative breast cancer (4T1 cells) and normal fibroblast cells.[119] Among the various approaches to SERS-based exosome detection, label-free strategies have gained attention due to their ability to preserve the vesicles' natural molecular signatures while simplifying the detection process. Unlike labeling techniques that require antibodies, aptamers, or chemical tags, label-free SERS allows direct molecular fingerprinting of exosomes, improving specificity and reducing sample preparation complexity. Fraire et al. developed a core–shell Au@Ag NP-based SERS approach that eliminates interference from stabilizing molecules by in situ silver overgrowth on exosome-bound gold NPs (**Figure** 8A).[120] This strategy significantly enhanced the signal-to-noise ratio and enabled single-vesicle identification with over 90% specificity. The same concept under a different approach was further explored by Park et al. by introducing a scalable laser-ablated silver NP (SLAM) substrate, enabling rapid and cost-effective fabrication of SERS platforms for high-throughput exosome detection.[121] This method enhances plasmonic effects through precisely engineered silver nanostructures, ensuring high sensitivity and reproducibility while facilitating large-scale analysis of cancer-derived ELVs. While both approaches demonstrate the potential of label-free SERS for liquid biopsy applications, the SLAM-based method offers a practical, high-throughput solution, whereas the core–shell strategy excels in single-exosome resolution, providing complementary tools for cancer diagnostics.

Recent advances in AI are pushing the boundaries of exosome-based liquid biopsies, enhancing both sensitivity and accuracy in cancer diagnostics. In that sense, Shin et al. developed an Exosome-SERS-AI platform that combines SERS with deep learning models to classify exosomes from patients with six different cancer types (lung, breast, colon, liver, pancreas, and stomach) (Figure 8B).[122] Their system first detects cancer presence with an accuracy of 90.2% and specificity of 94.4%, then predicts the tumor organ of origin with a mean AUC of 0.945. The AI model extracts subtle Raman spectral differences between cancerous and normal exosomes, enabling highly precise and non-invasive multi-cancer screening from a single test (Figure 8C).

Another interesting approach is the use of enzyme-driven MMs for exosome capture and transport. Liu et al. recently introduced a urease-powered MMs system for active exosome capture and transport before SERS analysis.[123] The self-propulsion capabilities depicted by these motors through the catalytic decomposition of urea significantly increased the efficiency of exosome isolation (improved binding efficiency by 35% compared to passive exosome collection methods). Once captured, exosomes are transferred to a clean environment for SERS-based molecular fingerprinting, ensuring high-precision diagnostics.

The development of high-throughput strategies for analyzing thousands of exosomes simultaneously is set to revolutionize their role in disease diagnosis and prognosis, particularly in cancer detection. Traditional methods often suffer from low

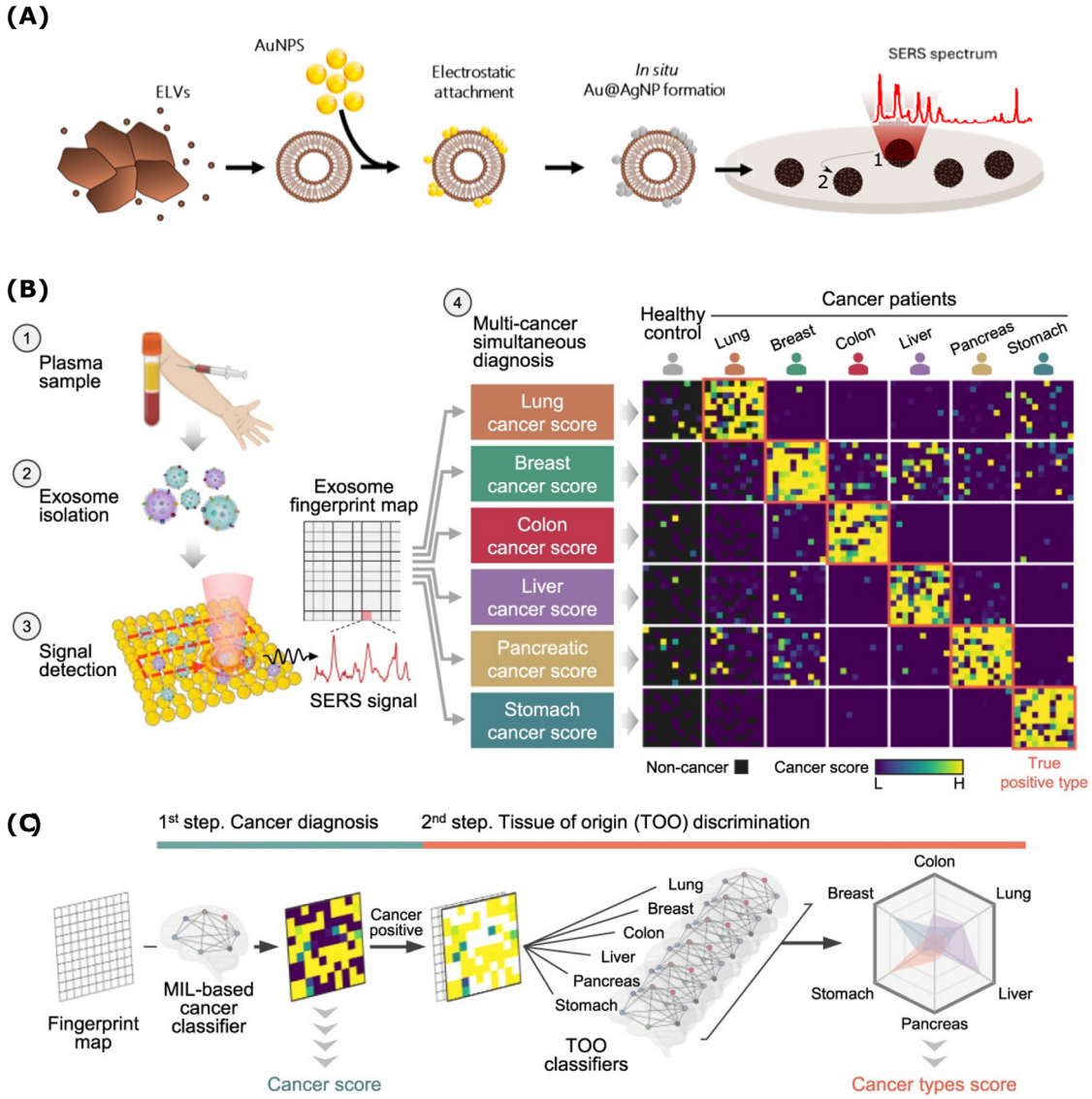

Figure 8. Surface-Enhanced Raman Spectroscopy (SERS) for Exosome-Based Cancer Diagnostics. A) In situ Au@AgNP formation as a strategy to obtain a clear spectral fingerprint of individual ELVs. Schematic representation of ligand-stabilized AuNP attached to the outer ELV surface and Au@AgNP in which the ligand coating is replaced by an outer silver layer. ELVs from B16F10 melanoma cells or red blood cells (RBCs) are electrostatically coated with 4-Dimethylaminopyridine (DMAP)-AuNPs (40% coverage); in situ functionalization with a silver layer around the ELV-attached DMAP–AuNPs; SERS spectra of individual ELVs deposited on a CaF_2 coverslip are recorded with a confocal Raman microscope. Reproduced or adapted with permission from ref.[120] Copyright 2019 American Chemical Society. B) One test-multi cancer using exosome-SERS-artificial intelligence (AI): Exosome suspension is dropped onto an Au NP-aggregated array chip and thoroughly dried; signals were observed at 100 spots (10 × 10) per sample and analyzed by AI algorithms; the system outputs predictions about cancer presence and tissue of origin; a heat map shows actual examples of the representative predicted results for each cancer status. Reproduced or adapted under the terms of the CC-BY license from ref.[122] Copyright 2023 Springer Nature. C) AI framework. In the first step, diagnostic scores are assigned as the mean values of the multiple instance learning (MIL)-based cancer classifier results. In the second step, signals predicted by the previous cancer classifier are analyzed, and then an average score is calculated using six types of prediction models. Reproduced or adapted in terms of the CC-BY license from ref.[122] Copyright 2023 Springer Nature.

throughput, complex sample preparation, and signal variability, limiting their clinical application. However, recent advancements in label-free substrates, single-particle Raman trapping, and AI-driven analysis are overcoming these challenges and paving the way for next-generation exosome-based diagnostics.

For instance, Penders et al. introduced the SPARTA (Single Particle Automated Raman Trapping Analysis) system, which enables label-free, high-throughput Raman screening of extracellular vesicles (EVs) at the single-particle level.[124,125] By analyzing over 14 000 individual EVs, SPARTA demonstrated the ability to differentiate between cancer and non-cancer EVs with >95% accuracy, providing a powerful tool for rapid, unbiased exosome characterization. Unlike conventional bulk SERS methods, SPARTA isolates and traps individual vesicles in solution, reducing background noise and improving spectral resolution. Future strategies will likely combine AI-powered analysis with novel

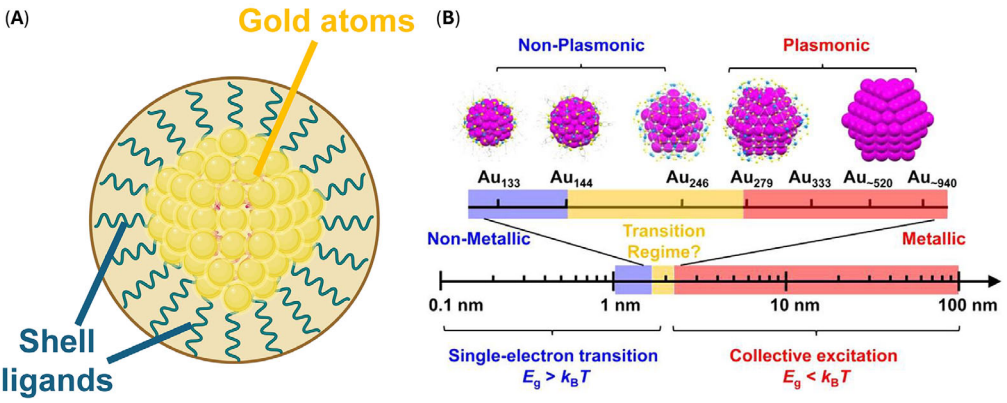

Figure 9. Gold nanoclusters (AuNCs) properties. A) Schematic representation of the core–shell structure of AuNCs. Created in BioRender. Sánchez, S. (2025) https://BioRender.com/feputnr. B) Schematic diagram of the band gap transition between AuNCs (non-metallic) and AuNPs (metallic) based on the number of gold atoms. Reproduced or adapted with permission from ref.[128] Copyright 2021 American Chemical Society.

SERS substrates and microfluidic trapping technologies, allowing real-time, high-throughput exosome profiling in clinical settings. The integration of plasmon-enhanced nanostructures for improved Raman signals, SPARTA for large-scale screening, and AI for spectral classification will enable rapid, noninvasive diagnostics for a range of diseases, from cancer to neurodegenerative disorders. Ultimately, we envision that these advancements could lead to the development of portable, automated liquid biopsy platforms, transforming exosome-based diagnostics from a research tool into routine clinical practice.

4. Gold Nanoclusters for Theragnostic

Unlike AuNPs, AuNCs consist of a few to a hundred gold atoms, with their photophysical properties dependent on the specific number of gold atoms (known as the "magic number"), and a size of less than 2 nm, forming a tightly arranged ultrasmall structure.[126] Similar to AuNPs, AuNCs require stabilization by organic ligands to form a core–shell structure (**Figure 9**A). Another key difference from AuNPs lies in their absorption properties. Meanwhile, AuNPs exhibit an LSPR peak; AuNCs do not put forward these absorption properties. Additionally, AuNCs display photoluminescence (PL) properties due to molecular transition between the highest occupied molecular orbital (HOMO) and the lowest unoccupied molecular orbitals (LUMO). In this regard, as the size of the AuNCS decreases, the separation between discrete energy levels grows, leading to a blue shift in the optical absorption of the AuNCs.[127,128] AuNCs have the ability to emit within visible light, NIR (700–900 nm) and shortwave infrared regions (SWIR) or NIR-II (1000–1700 nm), with their emission properties being tunable through size, crystal structure, and atomic packing, cluster charge state, and ligand nature (Figure 9B). Due to their PL properties and excellent biocompatibility, since gold is an inert noble metal, AuNCs have emerged as a promising tool for biomedical imaging. Furthermore, they offer greater photostability compared to commonly used organic dyes, along with a large Stokes shift and a long luminescence lifetime.[126,129] In this section, we explore how ligand chemistry governs the PL properties of AuNCs and discuss strategies to fine-tune their optical behavior. We also highlight the critical role of proteins as functional ligands in enhancing biocompatibility and targeting. Finally, we focus on AuNCs as versatile theragnostic agents, emphasizing their dual capabilities, i.e., diagnostic as fluorescent probes or sonosensitizers and therapeutic, such as PTT, photodynamic therapy (PDT), or drug/gene delivery systems.

4.1. Ligands for the Stabilization of Gold Nanoclusters

Ligands play a crucial role in stabilizing AuNCs, preventing their aggregation, and preserving their size-dependent fluorescence properties. Although the exact origin of AuNCs' photoluminescent properties remains controversial, it is well established that ligands significantly influence their optical properties. In fact, without stabilizing ligands, AuNCs remain non-fluorescent. These naked AuNCs, formed by simple reduction of gold salt with NaOH, can acquire fluorescence upon passivation with various thiols.[130] Therefore, the ligand plays a role in the PL properties, and it is believed that it is closely related to the charge transfer between the ligands and Au core (ligand–metal charge transfer, LMCT). Ligands transfer electrons to the gold, and this leads to an electronic transition and fluorescence emission. In other words, if the ligand is too small in size and contains few electron-rich atoms and groups, the cluster will not exhibit electron transfer and, in turn, not fluorescence as He et al. demonstrated with 3-mercaptopropionic acid (MPA).[131] Similar to AuNPs, AuNCs exhibit a strong affinity for thiol groups, making thiol-containing compounds excellent ligands for cluster stabilization (e.g., glutathione (GSH),[132] Lysine-Cysteine-Lysine (KCK),[131] 1-Thioglycerol (1-TG),[133] Cyclohexanethiolate (CHT),[134] PEG-SH),[135] even though other ligands have been reported, such as captopril,[136] 1,3-bis(diphenylphosphino)propane (dppp),[137] triphenylphosphonium (TPP).[138] The influence of the ligand properties and their interaction with gold on photoluminescence has been explored extensively. Thiolate ligands have been further studied, and it is pretty clear that they emit in the range of red or NIR, but the differences in wavelength and intensity at that range can be attributed to other factors, i.e., core size[139] (**Table 3**). However, the underlying mechanism remains unclear. Ramakrishna et al. showed that S-Au-Au-S semi-ring states are responsible for

Table 3. Photoluminescence properties and size of AuNCs synthesized using different ligands.

Capping ligand	Cluster size [nm]	λ_{em} [nm][a]	λ_{ex} [nm][b]	PLQY[c]	Refs.
Captopril	2	652	NA	NA	[136]
KCK[d]	2	700	405	NA	[131]
TPP[e]	1.15 ± 0.2	750	365	10–25%	[138]
GSH[f]	2–3	680	450	NA	[132]
PEG-SH[g]	NA	622	450	NA	[135]
1-TC[h]	NA	663	536	0.12%	[133]
CHT[i]	NA	784	372	1.6%	[134]
dppp[j]	1–2	700	510	0.02–0.27%	[137]
ATT[k]	NA	532	405	90.3±3.5%	[144]
Adm[l]	NA	800–900	550	10%	[145]

[a] Maximum wavelength emission; [b] Maximum wavelength excitation; [c] Photoluminescence quantum yield; [d] Lysine-Cysteine-Lysine; [e] Triphenylphosphonium; [f] Glutathione; [g] Polyethylene glycol; [h] 1-Thioglycerol; [i] Cyclohexanethiolate; [j] 1,3-bis(diphenylphosphino)propane; [k] 6-Aza-2-thiothymine; [l] 1-admantanethiolate.

Table 4. Properties and size of AuNCs synthesized using different protein templates.

Protein template	Cluster size [nm]	λ_{em} [nm][a]	λ_{ex} [nm][b]	PLQY[c]	Refs.
BSA[d]	0.8	640	470	6%	[155]
Trypsin	1–2	640	360	NA[e]	[156]
Lysozyme	1	657	360	5.6%	[157]
HSA[f]	–	655	368	NA	[158]
Insulin	0.92	670	400	4.0%	[159]
Pepsin	1–2	670	360	5.0%	[160]
Papain	6.7	639	490	NA	[161]
Peroxidase	2.7 ± 0.6	650	365	NA	[162]
CTPR[g]	1.5 ± 0.3	680	430–450	25 ± 2%	[154]
Enoyl-ACP reductase	1	627	366	4.68%	[163]
Transferrin	2.6 ± 0.5	710	380	7.7%	[164]
DNAse-1	1	460/640	395/460	NA	[165]
Keratin	NA	680	470	10.5%	[166]

[a] Maximum wavelength emission; [b] Maximum wavelength excitation; [c] Photoluminescence quantum yield; [d] Bovine serum albumin; [e] Not available; [f] Human serum albumin; [g] Consensus tetratricopeptides repeat protein.

the NIR luminescence of thiol-stabilized AuNCs.[140] In contrast, computational studies done by Aikens et al. suggest that both metal core size and surface chemistry play a crucial role and directly affect luminescence properties.[141] Other researchers propose that ligand density plays a key role in enhancing AuNCs' luminescence. Studies on glutathione (GSH)-stabilized AuNCs reveal a positive correlation between ligand density and luminescence intensity.[142,143]

Additionally, ligand length may also impact on PL. Zhang et al. demonstrated that the ligand structure affects both the stability and electronic properties of AuNCs. They further suggest that enhanced PL could result from improved encapsulation and protection of the gold core by ligands.[132] In this regard, the primary limitation or weakness of AuNCs for biomedical applications is their low PLQY, which significantly reduces the lifespan of their PL. Accordingly, Zhang et al. demonstrated that high PLQY can be achieved by suppressing metal core vibrations through sequential coating with 6-Aza-2-thiothymine (ATT), L-arginine (ARG), and tetraoctylammonium (TOA), which enhances surface rigidity via supramolecular interactions. The study achieved a record reporting a PLQY of 90.3% and 86.7% in toluene and water, respectively.[144]

In general, these studies suggest that the ligand has a key role in determining the PL properties of the nanomaterials, i.e., the type of interaction formed, ligand density around the gold core, and ligand length, which affects the LMCT. This implies that proper protection of the gold core from its surroundings is a *conditio sine qua non* to achieve enhanced properties. However, this also requires an electron-rich ligand capable of donating electrons to the gold core.

4.2. Protein Stabilization

Protein templates offer a significant advantage in nucleating and stabilizing precise AuNCs. Protein-stabilized AuNCs (Prot-AuNCs) have gained considerable attention due to their potential applications in biomedicine. Over the past decades, various proteins have been employed for this purpose. BSA was the first protein used as a template for AuNCs stabilization[146] and remains widely studied due to its high availability and low cost, with slight modifications in synthesis protocols influencing PL properties.[147–149] Unlike ligand-stabilized AuNCs, which require sodium borohydride ($NaBH_4$) as a reducing agent, the reductions are provided by the protein itself and high pH (≈12).[147] However, alternative methodologies for in situ formation of BSA-AuNCs have been explored, as $NaBH_4$ may alter the structure of the template protein.[150] In this context, green chemistry approaches include the self-reducing ability of the protein by changing pH (intrinsic method) or the addition of an external reducing agent as ascorbic acid (extrinsic method). Furthermore, physical methods, such as heating, microwave irradiation, or ultrasonic radiation, can be employed to activate the reducing power of the protein.[126,151,152] Since the introduction of BSA-AuNCs, numerous other proteins have been utilized for AuNCs growth, e.g., lysozyme, insulin, human serum albumin (HAS), trypsin, pepsin, and engineered proteins as consensus tetratricopeptide repeat (CTPR) protein.[153,154]

The PL properties of Prot-AuNCs are closely linked to the protein-AuNCs interaction (amino acid–metal complex), the environment provided by the protein template, and the AuNCs growth mechanism. While different proteins may slightly alter the emission properties of AuNCs, most exhibit a maximum emission peak in the red region (**Table 4**).

However, under specific conditions, the emission properties of AuNCS can be tuned, shifting the maximum emission wavelengths. Arakawa et al. were able to change the emission properties by means of changes in the pH of the medium. In an acidic environment (pH = 1), the emission shifts to 510 nm (green fluorescence) with a 3.5% PLQY under excitation of 330 nm. In contrast, in an alkaline environment (pH = 9), the emission shifts to 386 nm (blue fluorescence) with PLQY of 3.7% under excitation of 456 nm. They attributed these changes to the conformational

Table 5. AuNCs for biomedical applications.

Probe name	Application	λ_{em} [nm][a]	PLQY[b]	Refs.
BSA-Her[c]-AuNCs	Imaging and breast cancer therapy	640	NA	[174]
DHLA[d]-AuNCs	Monitoring Hg^{2+}	715	2.9%	[175]
W[e]-BSA-AuNCs	Imaging and drug delivery	480	7.13	[177]
PPI[f]-AuNCs	Cancer imaging	635	NA	[178]
LA[g]-sulfobetaine-AuNCs	Cancer imaging	1000	0.6–14.9%	[179]
BSA-AuNCs-DOX[h]	Imaging and drug delivery	659	1.9%	[181]
HA[i]-GSH[j]-AuNCs	Bioimaging-assisted cancer therapy	675	NA	[183]
BSA-AuNCs- MDDP[k]	Drug delivery and imaging	650–750	NA	[185]
AP1P2[l]-PEG NCs	Apoptosis-inducer and imaging	629	NA	[187]
GOx-CAT-HA[m]-siRNA CAuNCs[n]	Imaging and siRNA delivery	NA	NA	[188]
$Au_{25}(SG)_{18}$[o]	Monitoring cancer metastasis	1100–1700	4%	[189]
AuMHA[p]/TDT[q] NCs	Vascular disease	1250	6%	[190]
AuNC@HSA/CAT	Imaging and PDT[r]	600–650	NA	[170]
Au_{44}MBA[s]$_{26}$-Cy7[t]	NPTC[u]	1080–1280	NA	[172]

[a] Maximum wavelength emission; [b] Photoluminescence quantum yield; [c] Herceptin; [d] Dihydrolipoic acid; [e] Tryptophan; [f] Pea protein isolate; [g] Lipoic acid-based sulfobetaine; [h] Doxorubicin; [i] Hyaluronic acid; [j] Glutathione; [k] cis, cis, trans-$[Pt(NH_3)_2Cl_2(OH)(O_2CCH_2CH_2CO_2H)]$; [l] Amphipathic peptides (P1 and P2); [m] Hyaluronic acid; [n] Cationic AuNCs; [o] Glutathione; [p] Mercaptohexanoic acid; [q] Tetra(ethylene glycol) dithiol; [r] Photodynamic therapy; [s] 4-mercaptobenzoic acid; [t] Heptamethine; [u] Theranostics for cancer.

changes of the protein at the different pHs.[160] Interestingly, Cortajarena et al. designed a CTPR protein to modulate the fluorescence properties of AuNCs, highlighting the importance of the chemical environment surrounding the AuNCs.[167] On one hand, they demonstrated that the tryptophan (Trp) plays a key role in energy transfer between AuNCs. On the other hand, metal coordination modifies the properties, shifting the maximum emissions of the AuNCs.[154,167] In this sense, coordination with thiol groups provided by cysteine (Cys) residues results in completely different PL properties compared to coordination with histidine (His) residues.

In conclusion, Prot-AuNCs present certain advantages with respect to ligand-stabilizers, i.e., green synthesis and reduced toxicity. Moreover, they permit an easy tuning of the properties just by modifying the chemical properties of the protein. In contrast, it can potentially be recognized by the immune system, reducing the applicability of more than one time. As was displayed in most cases, the emission properties of both (ligand and Prot-based AuNCs) are focused on the red and NIR region, which can be limited to biomedical applications since this requires excitation light from the visible/UV region and thus produces tissue damage, and they have little deep into tissue. These issues can be overcome by working in SWIR, or "tissue-transparent window," as discussed in the next section.

4.3. Biomedical Applications of AuNCs

As demonstrated in previous sections, AuNCs exhibit exceptional optical properties that establish them as highly promising nanomaterials for both bioimaging applications and therapeutic platforms. Their unique characteristics enable diverse biomedical uses, including drug/gene delivery systems,[168] radiotherapy,[169] PDT,[170,171] and PTT.[172,173] Ligand-stabilized AuNCs have been widely employed in cellular imaging applications, including confocal microscopy and NIR fluorescent imaging (**Table 5**). Their inherent biocompatibility makes them particularly suitable for these purposes. For instance, Irudayaraj et al. employed BSA-AuNCs of ≈2 nm size, as a fluorescent contrast agent conjugated with Herceptin (a monoclonal antibody) for targeting and nuclear localization in human breast cancer cells over-expressing HER2 on the cell membrane (SKBR-3 cells) and tumor tissue (**Figure 10A**). This demonstrated their potential to cross the cell nucleus, enhancing and facilitating the therapeutic effect.[174] Nienhaus et al. advanced the use of AuNCs' fluorescent properties to sense changes in emission properties in the presence of Hg^{2+}. They synthesized NIR-emitting AuNCs stabilized by DHLA, which were internalized into the cells via endocytosis, providing an efficient method to monitor Hg^{2+} in living cells with a LOD of 0.5 nM.[175] Similarly, Shen et al. synthesized BSA-gold hybrid nanocubes (PGHNs) based on the assembly of BSA-AuNCs, demonstrating their high capacity to internalize in different types of cells as a cell marker (Figure 10B), i.e., *E. coli*, *Saccharomyces cerevisiae* (*S. cerevisiae*), and human embryonic kidney (HEK) 293, as well as their drug nanocarrier properties.[176] Moreover, the same group, based on the previous works, developed nanomaterials (PGHMs) with different optical properties by modifying the protein and free amino acids as stabilizers and reducing agents.[177] In contrast, Chen et al. employed proteins extracted from a plant (pea protein isolate, PPI) to stabilize AuNCs, acting as both a reducing and stabilizing agent. These AuNCs exhibited excellent fluorescent properties in the NIR and were applied as a bioimaging probe in vitro using human breast adenocarcinoma cells (MCF-7 cells) and in vivo coating PPI-AuNCs with red blood cells (RBC) membranes to facilitate the blood circulation and enhance the tumor enrichment, demonstrating successfully their location at the tumoral region (Figure 10C).[178] Bawendi et al. fabricated AuNCs stabilized with lipoic acid–based sulfobetaine (LA-sulfobetaine), where the PLQY could be tuned by adjusting the gold:ligand ratio, ranging from 0.6% to 14.9% with an increased ligand. They demonstrated the

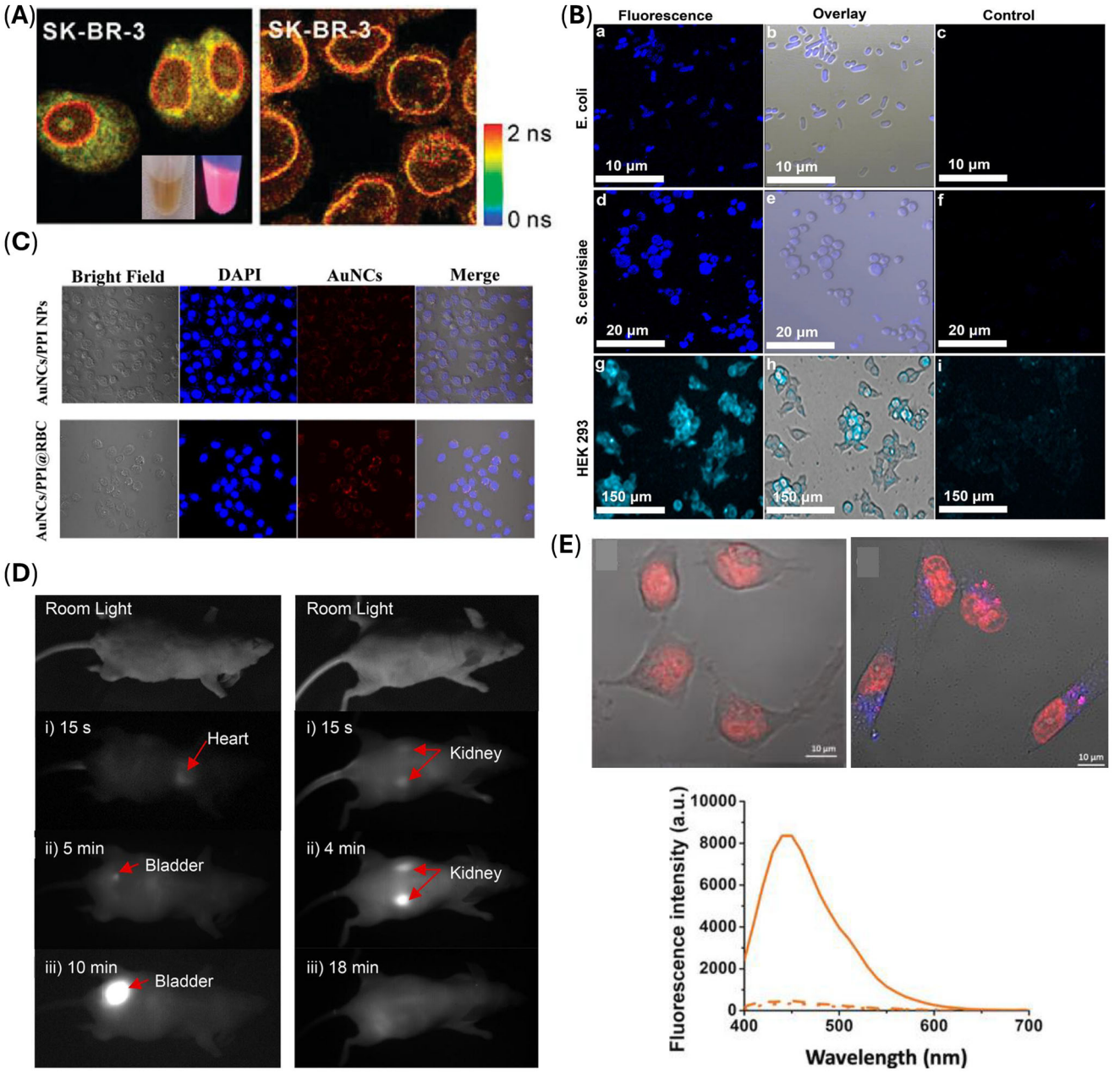

Figure 10. Cell imaging application of Protein-AuNCs. A) Fluorescence lifetime imaging (FLIM) of SK-BR3 cells stained by LaminA antibody labeled with Alexa350, indicating nuclear uptake of BSA-AuNCs-Her (left) and BSA-AuNCs alone (right). Reproduced or adapted with permission from ref.[174] Copyright 2011 American Chemical Society. B) Confocal fluorescent micrographs show that PGHNs entered E. coli, S. cerevisiae, and HEK 293 cells and emitted blue signals upon UV irradiation. Reproduced or adapted with the permission from ref.[176] Copyright 2015 American Chemical Society. C) Confocal images of MCF-7 cells incubated with AuNCs/PPI with or without RBC coating. Reproduced or adapted with the permission from ref.[178] Copyright 2017 American Chemical Society. D) Short-wavelength infrared images upon injection of AuNCs in a mice model. Reproduced or adapted with permission from ref180. Copyright 2017 American Chemical Society. E) Fluorescent spectra of AuNCs-CTPR (right) and live confocal fluorescence microscopy images (left) of MDA-MB-231 breast cancer cells incubated with CTPR (above) and AuNCs-CTPR (below). Reproduced or adapted under the terms of the CC-BY-NC 4.0 license from ref.[167] Copyright 2019 American Chemical Society.

potential of AuNCs for short-wavelength infrared (SWIR) imaging and showed efficient clearance of the AuNCs from mice due to their small size (Figure 10D).[179] Recently, Cortajarena et al. have worked with AuNCs-CTPR, showing their potential use in bioimaging of cancer cells (MDA-MB-231 breast cancer cells) (Figure 10E) and therapy on cardiac fibrosis.[167,180]

More importantly, many research groups have explored the idea of combining imaging and delivery systems simultaneously, creating a theragnostic platform that might include drug

release[181,182] and phototherapy.[183,184] Yaping et al. prepared BSA-AuNCs conjugated with cisplatin prodrug and folic acid for fluorescence imaging and chemotherapy of breast cancer. The authors claim that nanoformulation successfully accumulates in the breast tumor, inhibiting growth and metastasis, while avoiding accumulation in healthy organs, and efficiently monitoring the biodistribution simultaneously.[185] More recently, AuNCs have been used for the treatment of liver tumors. In this case, AuNCs were stabilized by GSH and peptides with the capacity to induce endoplasmic reticulum stress in liver cancer cells, triggering autophagy and apoptosis. Due to the presence of GSH as a capping of AuNCs, which is actively transported, the accumulation and uptake were enhanced inside the tumor.[186] The same group, led by Xingyu Jiang, was able to combine NIR fluorescence imaging, diagnosis, and treatment of lymph-node cancer metastasis in in vivo mouse models. They employed anionic alkylthiol ligands (zwitterionic) to stabilize the AuNCs, which resulted in effective accumulation in lymph node cancer and provided high-contrast fluorescent images. Moreover, chemotherapy therapy based on methotrexate was conjugated to AuNCs, showing excellent therapeutic efficacy and reduced toxicity compared to the free drug.[187]

By applying the extraordinary potential of AuNCs to monitor the biodistribution of therapy and self-propel nanomotors, the efficacy and precision of biomedicine could be significantly enhanced. Gao et al. utilized self-propelled nanomotors utilizing tandem reactions, i.e., glucose oxidase (GOx) and catalase, to modulate the hypoxic tumor microenvironment and inhibit glycolysis to prevent metastasis in triple-negative breast cancer. The enzymes were adsorbed onto AuNCs to form the aforementioned nanomotors. The final product of the enzymatic cascade generates oxygen that alleviates the tumor hypoxia. Moreover, the nanomotors were decorated with hexokinase-2 (HK-2) siRNA to silence aerobic glycolysis. Finally, they combined the therapy with paclitaxel, significantly reducing the metastasis.[188]

So far, the emission properties of the AuNCs discussed here are primarily centered in the red and NIR regions. However, the SWIR region is particularly advantageous, as it minimizes harmful radiation effects on the skin while enhancing light penetration depth, improving AuNCs tracking in biological systems. In this context, Xiao-Dong Zhang et al. successfully synthesized glutathione-stabilized Au_{25} clusters ($Au_{25}(SG)_{18}$) emitting in the NIR-II window (1100–1350 nm). This ultrasmall cluster (≈3.2 nm) enabled real-time monitoring of cancer metastasis, observing significant tumor uptake (**Figure 11A**). Moreover, ($Au_{25}(SG)_{18}$) exhibited efficient renal clearance (smaller than the threshold value of 5.5 nm), a feature shared with other similarly sized nanomaterials reviewed in this work.[189] In the same line, Xavier Le Guével et al. engineered SWIR-emitting AuNCs (1250 nm) via ligand modulation, using mercaptohexanoic acid (MHA) and tetra(ethylene glycol) dithiol (TDT) (AuMHA/TDT) to achieve a bright contrast agent with prolonged circulation in the vascular network (PLQY of ≈6%). They were able to detect fluorescent details down to >4 mm below the skin surface of mice (Figure 11B).[190] Yuan et al. developed a novel design of AuNCs ($Au_{44}MBA_{26}$-Cy7) for ultradeep NIR-II photoluminescence and photoacoustic imaging-guided cancer PTT, combining imaging-based diagnosis and photothermal therapy (Figure 11C). They demonstrated an enhanced NIR-II intensity and elevated photothermal efficiency.[172] More recently, Da et al. employed Au_{25} NCs stabilized with phosphorylcholine (AuPC) injected intratumorally for NIR-II imaging-guided resection of 4T1 murine breast cancer and as a PTT agent. They observed a uniform distribution of the AuPC within the tumoral area in less than 3 min after injection (Figure 11D). Moreover, they exploited the AuPC for PTT, demonstrating a decrease in the size of the tumor until complete eradication.[191] It is worth mentioning that AuNCs have additional exploitable properties, particularly their utility as radiosensitizers. Due to gold´s high atomic number, AuNCs significantly enhance radiotherapy efficacy by increasing X-ray absorption, which amplifies localized radiation dose deposition in target tissues.[192] In this context, Xie et al. reported a new class of radiosensitizers based on AuNCs stabilized with naturally occurring peptides and glutathione ($Au_{10-12}(SG)_{10-12}$), demonstrating highly efficient tumor uptake (**Figure 11E**). These nanoformulations could be employed as radiosensitizers to enhance the therapeutic efficiency of radiotherapy with gadolinium.[193] Recently, Faure et al. developed a multimodal cancer therapy platform utilizing AuNCs that simultaneously function as radiosensitizers and siRNA delivery vehicles. These nanomaterials combine NIR fluorescence with efficient cellular siRNA delivery while significantly enhancing radiosensitivity. When combined with X-ray irradiation, the system demonstrated a synergistic therapeutic effect, achieving a 2.3-fold increase in cancer cell death.[194]

To sum up, ligand- and protein-functionalized AuNCs have emerged as versatile tools for bioimaging, drug delivery, and theragnostic applications due to their biocompatibility, tunable fluorescence, and targeting capabilities. Studies demonstrate their effectiveness in cancer cell imaging (e.g., HER2-targeted SKBR-3 cells), Hg^{2+} sensing, and drug delivery (e.g., cisplatin prodrugs). Their small size enables efficient cellular uptake, nuclear localization, and enhanced tumor accumulation, as seen in breast and liver cancer models. Additionally, AuNCs have been integrated with NMs and enzyme cascades to modulate tumor microenvironments and improve therapeutic outcomes. On the other hand, controlling the Au core size is key to tuning the emission properties from red, NIR-I (700–900 nm) to SWIR/NIR-II (1000–1700 nm). AuNCs can be red-shifted to longer wavelengths by increasing the number of core gold atoms.[195] These advancements highlight AuNCs' potential in precision medicine, combining diagnostics and therapy for enhanced efficacy.

4.4. AuNCs for Theragnostic: Pitfalls and Challenges

As reviewed in the previous sections, we have explored the properties of AuNCs, including their atomic structure, ligand chemistry, and biomedical applications. Their exceptional potential as fluorescent probes for imaging and therapeutic approaches is evident. The small size of AuNCs facilitates efficient renal clearance, minimizing bioaccumulation, while their low toxicity enhances their suitability for biomedical use. Compared to alternative probes, AuNCs offer distinct advantages. Organic fluorescent probes often suffer from small Stokes shifts, leading to self-quenching and reduced accuracy in bioimaging.[196] Meanwhile, quantum dots (QDs), despite their bright emission, face challenges such as high toxicity (due to heavy metals like Cd^{2+})

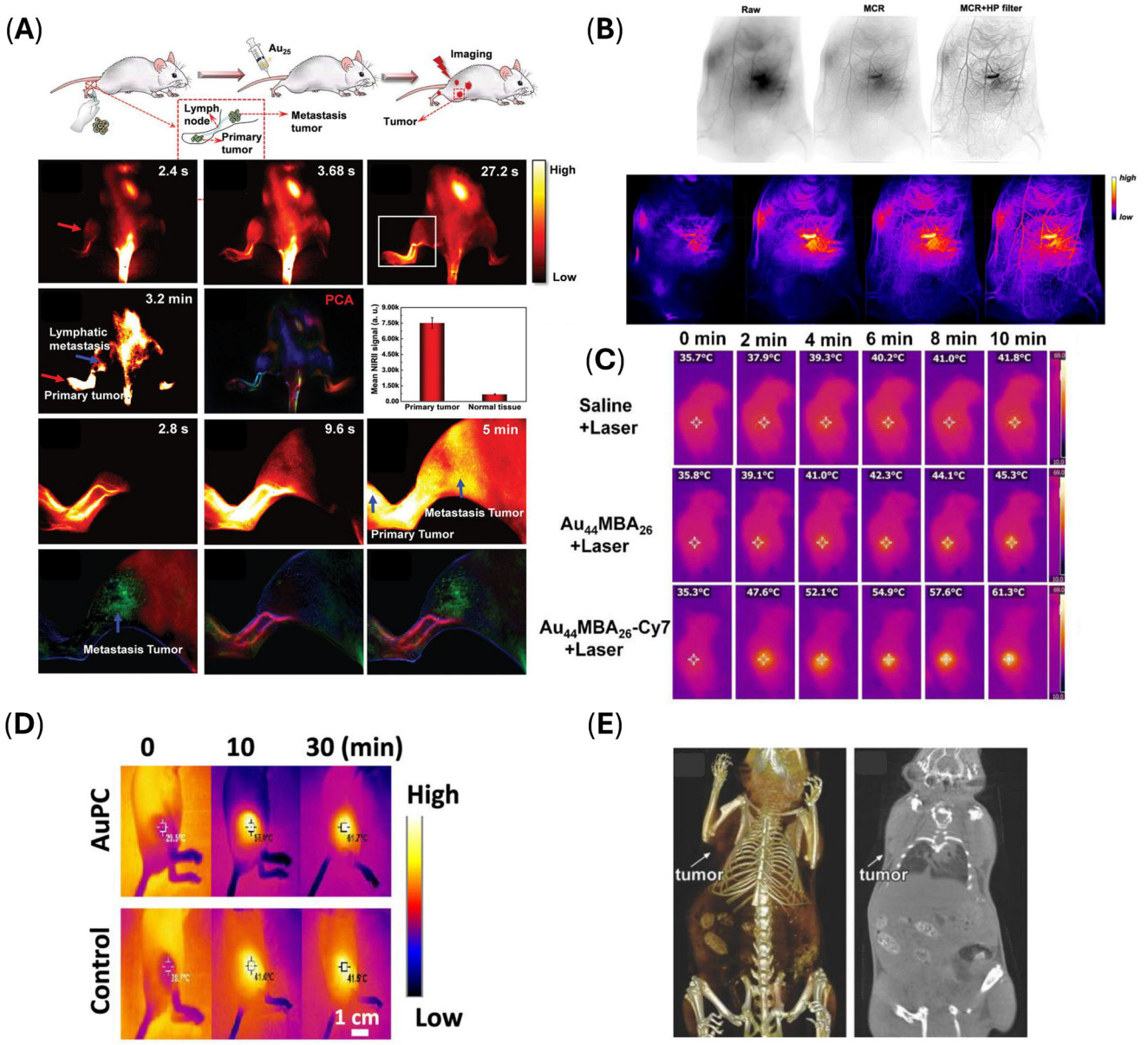

Figure 11. In vivo biomedical applications of AuNCs in SWIR. A) NIR-II imaging of tumor metastasis through intravenous injection of $Au_{25}(SG)_{18}$. Reproduced or adapted with permission from ref.[189] Copyright 2019 John Wiley and Sons. B) Vascular distribution of AuMHA/TDT in mice injected. Reproduced or adapted with permission from ref.[190] Copyright 2020 American Chemical Society. C) Photothermal images of tumor-bearing mice injected intravenously with the $Au_{44}MBA_{26}$-Cy7 NCs. Reproduced or adapted under the terms of the CC-BY-NC 3.0 license from ref.[172] Copyright 2023 Royal Society of Chemistry. D) Photothermal images showing the biodistribution and temperature of Au_{25} NCs stabilized with phosphorylcholine (AuPC). Reproduced or adapted under the terms of CC-BY-NC-ND 4.0 license from ref.[191] Copyright 2023 United States National Academy of Sciences. E) X-ray computed tomography (CT) images of $Au_{10-12}(SG)_{10-12}$ biodistribution. Reproduced or adapted with permission from ref.[192] Copyright 2014 John Wiley and Sons.

and instability in physiological environments, limiting their clinical applicability.[197] In contrast, AuNCs combine large Stokes shifts, excellent biocompatibility, and tunable emission, making them a superior choice for sensitive and precise bioimaging applications.[198]

However, several challenges remain. First, our ability to precisely control the optical properties of AuNCs is still limited. To fully exploit their potential, we must develop strategies to extend their emission beyond the visible and NIR-I regions into the tissue-transparent NIR-II/SWIR window (1000–1700 nm), where deeper light penetration (>1 cm) and reduced scattering enable higher-resolution imaging with minimal tissue damage.[172] Another critical challenge is the low PLQY of AuNCs, primarily due to non-radiative transitions induced by ligand-related electronic states. To address this, some strategies should be investigated, e.g., engineering the ligands on the gold surface, modifying the gold core size, composition of the metals, aggregation-induced enhancement, surface shell rigidification, self-assembling

strategies, and regulating the ambient conditions (temperature or solvents).

5. Conclusions and Future Outlook

Recent advancements in nanotechnology have driven the development of multifunctional photonic nanomaterials for theragnostic applications with unprecedented precision. Among them, AuNPs and AuNCs stand out for their versatility in bioimaging, biosensing, and therapy. The optical properties of AuNPs, governed by LSPR, have revolutionized techniques such as SERS for bioimaging and PTT for targeted treatment. Meanwhile, AuNCs, with their tunable PL and superior biocompatibility, have opened new avenues for biomarker detection and ROS-based therapies.

Beyond their conventional applications, the integration of AuNPs into NMs has enhanced active matter technology, enabling precise in vivo tracking and the visualization of plasmonic NMs in bladder tumors. More recently, these plasmonic properties have been harnessed to implement PTT in NMs, achieving localized ablation of tumor cells after penetration into pathological tissues.

Looking ahead, the future of plasmonic nanomaterials hinges on their refinement for clinical translation. Advances in surface chemistry and ligand engineering will be key for ensuring NPs stability, minimizing the absorption of proteins (PC effect), and enhancing targeted delivery. In the era of AI-driven innovation, integrating AuNPs and AuNCs with machine learning algorithms will accelerate optimization, addressing current limitations and unlocking their full potential in biomedical applications.

Emerging research on hybrid nanostructures, such as gold-based nanocomposites with biodegradable polymers, is set to enhance biocompatibility and better biodistribution. Additionally, the integration of plasmonic nanomaterials with advanced imaging technologies, photoacoustic imaging, and super-resolution microscopy will push the boundaries of real-time diagnostics and therapeutic monitoring, refining precision in biomedical applications.

Lastly, the integration of plasmonic nanomaterials into active matter, particularly NMs, exhibits a promising frontier in precision medicine. The synergy between AuNP-functionalized NMs for targeted delivery and their role in advanced therapies such as PTT will overcome current limitations, paving the way for more effective disease detection, precision therapy, and minimally invasive interventions.

Acknowledgements

This work had received funding from the grant PID2021-128417OB-I00 funded by MCIN/AEI/ 10.13039/501100011033 and "ERDF A way of making Europe" and European Union Next Generation EU/PRTR (Bots4BB project), the CERCA program by the Generalitat de Catalunya, Secretaria d'Universitats i Recerca del Departament d'Empresa i Coneixement de la Generalitat de Catalunya through the project 2021 SGR 01606, and the Centro de Excelencia Severo Ochoa CEX2023-001282-S, funded by MICIU/AEI/ 10.13039/501100011033. This project has also received funding from the European Research Council (ERC) under the European Union's Horizon 2020 research and innovation program (grants agreement No. 866348, i-NanoSwarms, 101138723, MucOncoBots, and 101189423, OrthoBots), from "la Caixa" Foundation under the grant agreement LCF/PR/HR21/52410022 (BLADDEBOTS), and "Fundación BBVA" under the Becas Leonardo 2024. J.C.F. acknowledges the Beatriu de Pinós Programme (2021-BP-00079), the Ministry of Business and Knowledge of the Government of Catalonia. D.S.d.A. acknowledges financial support from the MCIN/AEI through the Juan de la Cierva grant FJC2021-048024-I, and the Torres Quevedo grant PTQ2023-013272. S.S. also acknowledges the "Constantes y Vitales" 2023 prize.

Conflict of Interest

The authors declare no conflict of interest.

Keywords

gold nanoparticles, nanoclusters, nanomotors, plasmonic biosensors, SERS

Received: January 31, 2025
Revised: June 16, 2025
Published online: July 14, 2025

[1] C. N. R. Rao, S. R. C. Vivekchand, K. Biswas, A. Govindaraj, *Dalton Trans.* **2007**, *2007*, 3728.
[2] J. J. Giner-Casares, M. Henriksen-Lacey, M. Coronado-Puchau, L. M. Liz-Marzán, *Mater. Today* **2016**, *19*, 19.
[3] R. D. Tweney, *Perspect. Sci.* **2006**, *14*, 97.
[4] I. Venditti, *Materials* **2017**, *10*, 97.
[5] H. Duman, F. Eker, E. Akdaşçi, A. M. Witkowska, M. Bechelany, S. S. N. Karav, *Nanomaterials* **2024**, *14*, 1527.
[6] J. C. Fraire, E. A. Coronado, *Nanobiomater. Med. Imaging: Appl. Nanobiomater.* **2016**, *8*, 131.
[7] V. Amendola, R. Pilot, M. Frasconi, O. M. Maragò, M. A. Iatì, *J. Phys.: Condens. Matter* **2017**, *29*, 203002.
[8] N. Elahi, M. Kamali, M. H. Baghersad, *Talanta* **2018**, *184*, 537.
[9] A. Gupta, D. F. Moyano, A. Parnsubsakul, A. Papadopoulos, L.-S. Wang, R. F. Landis, R. Das, V. M. U Rotello, B. G. Nanoparticles, *ACS Appl. Mater. Interfaces* **2016**, *8*, 14096.
[10] R. Lévy, N. T. K. Thanh, R. C. Doty, I. Hussain, R. J. Nichols, D. J. Schiffrin, M. Brust, D. G. Fernig, *J. Am. Chem. Soc.* **2004**, *126*, 10076.
[11] C. Simó, M. Serra-Casablancas, A. C. Hortelao, V. Di Carlo, S. Guallar-Garrido, S. Plaza-García, R. M. Rabanal, P. Ramos-Cabrer, B. Yagüe, L. Aguado, L. Bardia, S. Tosi, V. Gómez-Vallejo, A. Martín, T. Patiño, E. Julián, J. Colombelli, J. Llop, S. Sánchez, *Nat. Nanotechnol.* **2024**, *19*, 554.
[12] R. S. Riley, E. S. Day, *WIREs Nanomed. Nanobiotechnol.* **2017**, *9*, 1449.
[13] N. N. Nedyalkov, A. O. Dikovska, I. Dimitrov, R. Nikov, P. A. Atanasov, R. A. Toshkova, E. G. Gardeva, L. S. Yossifova, M. T. Alexandrov, *Quantum Elec.* **2012**, *42*, 1123.
[14] L. Yang, P. Hou, J. Wei, B. Li, A. Gao, Z. Yuan, *Molecules* **2024**, *29*, 1574.
[15] H. Qian, M. Zhu, Z. Wu, R. Jin, *Acc. Chem. Res.* **2012**, *45*, 1470.
[16] D. M. Chevrier, *J. Nanophotonics* **2012**, *6*, 064504.
[17] Y. Xia, N. J. Halas, *MRS Bull.* **2005**, *30*, 338.
[18] J. Georgeous, N. AlSawaftah, W. H. Abuwatfa, G. A. Husseini, *Pharmaceutics* **2024**, *16*, 1332.
[19] J. Kimling, M. Maier, B. Okenve, V. Kotaidis, H. Ballot, A. Plech, *J. Phys. Chem. B* **2006**, *110*, 15700.
[20] M. D'Acunto, *Materials* **2018**, *11*, 882.
[21] H. Yuan, C. G. Khoury, H. Hwang, C. M. Wilson, G. A. Grant, T. G. N. Vo-Dinh, *Nanotechnology* **2012**, *23*, 075102.

[22] H. Alvandi, A. H. Rezayan, H. Hajghassem, F. Rahimi, *Talanta* **2025**, *283*, 127184.
[23] X. Yang, J. Guo, F. Yang, G. Yang, Y. Wu, Z. Li, Y. Liu, X. Yang, J. Yao, *Sens Actuators B Chem* **2025**, *426*, 136986.
[24] Y. Ahmed, T. Akter, M. Prima, K. R. Dutta, S. Mukut, M. Ahsan, M. M. Rahman, M. K. Mohammad Ziaul Hyder, *J. Environ. Chem. Eng.* **2025**, *13*, 115094.
[25] P. S. Valera, M. Henriques-Pereira, M. Wagner, V. M. Gaspar, J. F. Mano, L. M. Liz-Marzán, *ACS Sens.* **2024**, *9*, 4236.
[26] E. Ha, H. Kang, H. Noh, *Biosensors* **2025**, *15*, 16.
[27] B. Tadgell, C. García-Astrain, M. Henriksen-Lacey, V. F. Martín, M. Obelleiro-Liz, L. M. Liz-Marzán, *J. Am. Chem. Soc.* **2025**, *147*, 2860.
[28] C. Renero-Lecuna, K. R. Pulagam, K. B. Uribe, P. Vázquez-Aristizabal, V. Gómez-Vallejo, L. M. Liz-Marzán, J. Llop, M. Henriksen-Lacey, *Part. Part. Syst. Charact.* **2024**, *41*, 2400185.
[29] Y. Zhong, X. Li, L. Ye, P. Zhu, L. Zhuang, *J. Mater. Chem. C Mater.* **2025**, *13*, 3606.
[30] C. Kuttner, V. Piotto, L. M. Liz-Marzán, *Chem. Mater.* **2021**, *33*, 8904.
[31] D. Jimenez De Aberasturi, A. B. Serrano-Montes, J. Langer, M. Henriksen-Lacey, W. J. Parak, L. M. Liz-Marzán, *Chem. Mater.* **2016**, *28*, 6779.
[32] M. Negahdary, M. Behjati-Ardakani, N. Sattarahmady, H. Yadegari, H. Heli, *Sens. Actuators B Chem.* **2017**, *252*, 62.
[33] X. Wu, T. Ming, X. Wang, P. Wang, J. Wang, J. Chen, *ACS Nano* **2010**, *4*, 113.
[34] T. N. Huan, T. Ganesh, K. S. Kim, S. Kim, S. H. Han, H. Chung, *Biosens. Bioelectron.* **2011**, *27*, 183.
[35] S. A. Bansal, V. Kumar, J. Karimi, A. P. Singh, S. Kumar, *Nanosc. Adv.* **2020**, *2*, 3764.
[36] H. Kang, J. T. Buchman, R. S. Rodriguez, H. L. Ring, J. He, K. C. Bantz, C. L. Haynes, *Chem. Rev.* **2019**, *119*, 664.
[37] Q. Ong, Z. Luo, F. Stellacci, *Acc. Chem. Res.* **2017**, *50*, 1911.
[38] D. Esporrín-Ubieto, C. Huck-Iriart, A. S. Picco, A. Beloqui, M. Calderón, *Small* **2024**, *20*, 2404097.
[39] P. Wang, X. Wang, L. Wang, X. Hou, W. Liu, C. Chen, *Sci. Technol. Adv. Mater.* **2015**, *16*, 034610.
[40] M. Wagner, A. Herrero-Ruiz, E. Verde-Sesto, I. Asenjo-Sanz, L. M. Liz-Marzán, *Chem. Mater.* **2025**, *37*, 644.
[41] A. A. Serkov, M. E. Shcherbina, P. G. Kuzmin, N. A. Kirichenko, *Appl. Surf. Sci.* **2015**, *336*, 96.
[42] A. Pedrazo-Tardajos, N. Claes, D. Wang, A. Sánchez-Iglesias, P. Nandi, K. Jenkinson, R. De Meyer, L. M. Liz-Marzán, S. Bals, *Nat. Chem.* **2024**, *16*, 1278.
[43] T. Bewersdorff, E. A. Glitscher, J. Bergueiro, M. Eravci, E. Miceli, A. Haase, M. Calderón, *Mater. Sci. Eng., C* **2020**, *117*, 111270.
[44] N. Dridi, Z. Jin, W. Perng, H. Mattoussi, *ACS Nano* **2024**, *18*, 8649.
[45] J. Nam, N. Won, H. Jin, H. Chung, S. Kim, *J. Am. Chem. Soc.* **2009**, *131*, 13639.
[46] A. Rao, A. S. Iglesias, M. Grzelczak, *J. Am. Chem. Soc.* **2024**, *146*, 18236.
[47] X. Wang, T. Yang, Z. Yu, T. Liu, R. Jin, L. Weng, Y. Bai, J. J. Gooding, Y. Zhang, X. Chen, *Adv. Mater.* **2022**, *34*, 2110219.
[48] J. Chen, Y. Ma, W. Du, T. Dai, Y. Wang, W. Jiang, Y. Wan, Y. Wang, G. Liang, G. Wang, *Adv. Funct. Mater.* **2020**, *30*, 2001566.
[49] M. Sun, D. Peng, H. Hao, J. Hu, D. Wang, K. Wang, J. Liu, X. Guo, Y. Wei, W. Gao, *ACS Appl. Mater. Interfaces* **2017**, *9*, 10453.
[50] X. Cheng, R. Sun, L. Yin, Z. Chai, H. Shi, M. Gao, *Adv. Mater.* **2017**, *29*, 1604894.
[51] G. G. Carbone, S. Mariano, A. Gabriele, S. Cennamo, V. Primiceri, M. R. Aziz, E. Panzarini, L. Calcagnile, *Pharmaceutics* **2025**, *17*, 176.
[52] Y. Yue, A. Moriyama, M. Mita, Y. Yu, *ChemPlusChem* **2025**, 2400783.
[53] M. Kodiha, Y. M. Wang, E. Hutter, D. Maysinger, U. Stochaj, *Theranostics* **2015**, *5*, 357.
[54] Y. Yang, L. Ren, H. Wang, *Ther. Deliv.* **2017**, *8*, 879.
[55] J. W. Kang, P. T. C. So, R. R. Dasari, D.-K Lim, *Nano Lett.* **2015**, *15*, 1766.
[56] Y. Shen, L. Liang, S. Zhang, D. Huang, R. Deng, J. Zhang, H. Qu, S. Xu, C. Liang, W. Xu, *ACS Appl. Mater. Interfaces* **2018**, *10*, 7910.
[57] B. Kepsutlu, V. Wycisk, K. Achazi, S. Kapishnikov, A. J. Pérez-Berná, P. Guttmann, A. Cossmer, E. Pereiro, H. Ewers, M. Ballauff, G. Schneider, J. G. McNally, *ACS Nano* **2020**, *14*, 2248.
[58] M. W. Helal, M. M. Faried, S. M. Salah, M. Ashraf, N. Nasser, Y. Shawky, S. Hamdy, A. E. Amir, W. Nabil, D. M El-Husseini, *Appl. Biochem. Biotechnol.* **2025**, *197*, 1678.
[59] Y.-C. Chen, L.-C. Chang, Y.-L. Liu, M.-C. Chang, Y.-F. Liu, P.-Y. Chang, D. Manoharan, W.-J. Wang, J.-S. Chen, H.-C. Wang, W.-T. Chiu, W.-P. Li, H.-S. Sheu, W.-P. Su, C.-S. Yeh, *Nat. Commun.* **2025**, *16*, 3253.
[60] L. Fan, W. Wang, Z. Wang, M. Zhao, *Nat. Commun.* **2021**, *12*, 6371.
[61] G. Yuan, X. Luo, K. He, Y. Tan, C. Luo, B. Liu, Y. Sun, J. Liu, *Sci. Adv.* **2025**, *11*, 7032.
[62] N. Ruiz-González, D. Esporrín-Ubieto, I.-D. Kim, J. Wang, S. Sánchez, *ACS Nano* **2025**, *19*, 8411.
[63] N. Ruiz-González, D. Esporrín-Ubieto, A. C. Hortelao, J. C. Fraire, A. C. Bakenecker, M. Guri-Canals, R. Cugat, J. M. Carrillo, M. Garcia-Batlletbó, P. Laiz, T. Patiño, S. Sánchez, *Small* **2024**, *20*, 2309387.
[64] J. C. Fraire, M. Guix, A. C. Hortelao, N. Ruiz-González, A. C. Bakenecker, P. Ramezani, C. Hinnekens, F. Sauvage, S. C. De Smedt, K. Braeckmans, S. Sánchez, *ACS Nano* **2023**, *17*, 7180.
[65] M. Serra-Casablancas, V. Di Carlo, D. Esporrín-Ubieto, C. Prado-Morales, A. C. Bakenecker, S. Sánchez, *ACS Nano* **2024**, *18*, 16701.
[66] D. Schamel, A. G. Mark, J. G. Gibbs, C. Miksch, K. I. Morozov, A. M. Leshansky, P. Fischer, *ACS Nano* **2014**, *8*, 8794.
[67] A. Aghakhani, A. Pena-Francesch, U. Bozuyuk, H. Cetin, P. Wrede, M. Sitti, *Sci. Adv.* **2022**, *8*, 5126.
[68] W. Liu, W. Wang, X. Dong, Y. Sun, *ACS Appl. Mater. Interfaces* **2020**, *12*, 12618.
[69] A. C. Hortelao, C. Simó, M. Guix, S. Guallar-Garrido, E. Julián, D. Vilela, L. Rejc, P. Ramos-Cabrer, U. Cossío, V. Gómez-Vallejo, T. Patiño, J. Llop, S. Sánchez, *Sci. Robot.* **2021**, *6*, abd2823.
[70] A. Bazrafshan, M.-E. Kyriazi, B. A. Holt, W. Deng, S. Piranej, H. Su, Y. Hu, A. H. El-Sagheer, T. Brown, G. A. Kwong, A. G. Kanaras, K. Salaita, *ACS Nano* **2021**, *15*, 8427.
[71] H. Šípová, L. Shao, N. Odebo Länk, D. Andrén, M. Käll, *ACS Photonics* **2018**, *5*, 2168.
[72] S. Liu, D. Xu, J. Chen, N. Peng, T. Ma, F. Liang, *Nanoscale* **2023**, *15*, 12944.
[73] H. Wang, J. Gao, C. Xu, Y. Jiang, M. Liu, H. Qin, Y. Ye, L. Zhang, W. Luo, B. Chen, L. Du, F. Peng, Y. Li, Y. Tu, *Small* **2024**, *20*, 2306208.
[74] J. Wang, H. Wu, X. Zhu, R. Zwolsman, S. R. J. Hofstraat, Y. Li, Y. Luo, R. R. M. Joosten, H. Friedrich, S. Cao, L. K. E. A. Abdelmohsen, J. Shao, J. C. M. van Hest, *Nat. Commun.* **2024**, *15*, 4878.
[75] S. Cao, J. Shao, H. Wu, S. Song, M. T. De Martino, I. A. B. Pijpers, H. Friedrich, L. K. E. A. Abdelmohsen, D. S. Williams, J. C. M. van Hest, *Nat. Commun.* **2021**, *12*, 2077.
[76] W. Guo, Y. Wang, K. Zhang, X. Dai, Z. Qiao, Z. Liu, B. Yu, N. Zhao, F.-J. Xu, *Chem. Mater.* **2023**, *35*, 6853.
[77] M. Fränzl, F. Cichos, *Nat. Commun.* **2022**, *13*, 656.
[78] D. J. Simon, F. Hartmann, T. Thalheim, F. Cichos, *Macromol. Chem. Phys.* **2023**, *224*, 2300060.
[79] J. C. Fraire, E. A. Coronado in *Nanobiomaterials in Medical Imaging*, Elsevier Inc., Amsterdam, Netherlands, **2016**, pp. 131–162.
[80] C. J. Murphy, A. M. Gole, J. W. Stone, P. N. Sisco, A. M. Alkilany, E. C. Goldsmith, S. C. G Baxter, *Acc. Chem. Res.* **2008**, *41*, 1721.
[81] J. N. Anker, W. P. Hall, O. Lyandres, N. C. Shah, J. Zhao, R. P. Van Duyne, *Nat. Mater.* **2008**, *7*, 442.

[82] C. Sönnichsen, B. M. Reinhard, J. Liphardt, A. P. Alivisatos, *Nat. Biotechnol.* **2005**, *23*, 741.
[83] B. Sepúlveda, P. C. Angelomé, L. M. Lechuga, L. M. Liz-Marzán, *Nano Today* **2009**, *4*, 244.
[84] E. A. Coronado, R. Encina, F. D. Stefani, *Nanoscale* **2011**, *3*, 4042.
[85] K. L. Kelly, E. Coronado, L. L. Zhao, G. C. Schatz, *J. Phys. Chem. B* **2003**, *107*, 668.
[86] C. F. Bohrem, D. R. Huffman in *Absorption and Scattering of Light by Small Particles*, John Wiley & Sons, New York, **1998**, pp. 1–530.
[87] J. Satija, N. Punjabi, D. Mishra, S. Mukherji, *RSC Adv.* **2016**, *6*, 85440.
[88] X. Yang, Z. Gao, *Chem. Commun.* **2015**, *51*, 6928.
[89] J. Liang, C. Yao, X. Li, Z. Wu, C. Huang, Q. Fu, C. Lan, D. Cao, Y. Tang, *Biosens. Bioelectron.* **2015**, *69*, 128.
[90] R. De La Rica, M. M. Stevens, *Nat. Nanotechnol.* **2012**, *7*, 821.
[91] Z. Xuan, M. Li, P. Rong, W. Wang, Y. Li, D. Liu, *Nanoscale* **2016**, *8*, 17271.
[92] J. C. Fraire, R. D. Motrich, E. A. Coronado, *Nanoscale* **2016**, *8*, 17169.
[93] S. Zhang, A. Garcia-D'Angeli, J. P. Brennan, Q. Huo, *Analyst* **2013**, *139*, 439.
[94] P. A. Mercadal, J. C. Fraire, R. D. Motrich, E. A. Coronado, *ACS Omega* **2018**, *3*, 2340.
[95] G. A. López-Muñoz, M. C. Estevez, E. C. Peláez-Gutierrez, A. Homs-Corbera, M. C. García-Hernandez, J. I. Imbaud, L. M. Lechuga, *Biosens. Bioelectron.* **2017**, *96*, 260.
[96] M. Soler, M. C. Estevez, R. Villar-Vazquez, J. I. Casal, L. M. Lechuga, *Anal. Chim. Acta* **2016**, *930*, 31.
[97] A. Losoya-Leal, M. C. Estevez, S. O. Martínez-Chapa, L. M. Lechuga, *Talanta* **2015**, *141*, 253.
[98] O. Calvo-Lozano, M. Sierra, M. Soler, M. C. Estévez, L. Chiscano-Camón, A. Ruiz-Sanmartin, J. C. Ruiz-Rodriguez, R. Ferrer, J. J. González-López, J. Esperalba, C. Fernández-Naval, L. Bueno, R. López-Aladid, A. Torres, L. Fernández-Barat, S. Attoumani, R. Charrel, B. Coutard, *Anal. Chem.* **2022**, *94*, 975.
[99] J. Treviño, A. Calle, J. M. Rodríguez-Frade, M. Mellado, L. M. Lechuga, *Clin. Chim. Acta* **2009**, *403*, 56.
[100] E. R. Encina, E. A. Coronado, *J. Phys. Chem. C* **2011**, *115*, 15908.
[101] E. R. Encina, E. A. Coronado, *J. Phys. Chem. C* **2010**, *114*, 3918.
[102] E. M. Perassi, L. R. Canali, E. A. Coronado, *J. Phys. Chem. C* **2009**, *113*, 6315.
[103] J. C. Fraire, L. A. Pérez, E. A. Coronado, *ACS Nano* **2012**, *6*, 3441.
[104] J. C. Fraire, L. A. Pérez, E. A. Coronado, *J. Phys. Chem. C* **2013**, *117*, 23090.
[105] X. S. Zheng, C. Zong, X. Wang, B. Ren, *Anal. Chem.* **2019**, *91*, 8383.
[106] S. Kumar, A. Kumar, G. H. Kim, W. K. Rhim, K. L. Hartman, J. M. Nam, *Small* **2017**, *13*, 1701584.
[107] J. C. Fraire, M. L. Masseroni, I. Jausoro, E. M. Perassi, A. M. Diaz Anel, E. A. Coronado, *ACS Nano* **2014**, *8*, 8942.
[108] A. Jaworska, L. E. Jamieson, K. Malek, C. J. Campbell, J. Choo, S. Chlopicki, M. Baranska, *Analyst* **2015**, *140*, 2321.
[109] J. Guo, A. Sesena Rubfiaro, Y. Lai, J. Moscoso, F. Chen, Y. Liu, X. Wang, J. He, *Analyst* **2020**, *145*, 4852.
[110] Y. Zhang, D. J. de Aberasturi, M. Henriksen-Lacey, J. Langer, L. M. Liz-Marzan, *ACS Sens.* **2020**, *5*, 3194.
[111] L. E. Jamieson, A. Jaworska, J. Jiang, M. Baranska, D. J. Harrison, C. J. Campbell, *Analyst* **2015**, *140*, 2330.
[112] S. Zhang, L. Ji, K. Xu, X. Xiong, B. Ai, W. Qian, J. Dong, *Anal. Methods* **2024**, *16*, 3263.
[113] H. Y. Chen, Y. He, X. Y. Wang, M. J. Ye, C. Chen, R. C. Qian, D. W. Li, *Talanta* **2025**, *284*, 127222.
[114] Y. Shen, L. Liang, J. Zhang, Z. Li, J. Yue, J. Wang, W. Xu, W. Shi, S. Xu, *Sens Actuators B Chem* **2019**, *285*, 84.
[115] Y. Yang, S. Wu, Y. Chen, H. Ju, *Chem. Sci.* **2023**,*14*, 12869.
[116] W. Zhang, F. Lin, Y. Liu, H. Zhang, T. A. Gilbertson, A. Zhou, *Proc. Natl. Acad. Sci. USA* **2020**, *117*, 3518.
[117] Z. Wang, S. Zong, Y. Wang, N. Li, L. Li, J. Lu, Z. Wang, B. Chen, Y. Cui, *Nanoscale* **2018**, *10*, 9053.
[118] S. Stremersch, M. Marro, B.-E. Pinchasik, P. Baatsen, A. Hendrix, S. C. De Smedt, P. Loza-Alvarez, A. G. Skirtach, K. Raemdonck, K. Braeckmans, *Small* **2016**, *12*, 3292.
[119] X. Li, M. Keshavarz, P. Kassanos, Z. Kidy, A. Roddan, E. Yeatman, A. J. Thompson, *Adv. Sens. Res.* **2023**, *2*, 2200039.
[120] J. C. Fraire, S. Stremersch, D. Bouckaert, T. Monteyne, T. De Beer, P. Wuytens, R. De Rycke, A. G. Skirtach, K. Raemdonck, S. De Smedt, K. Braeckmans, *ACS Appl. Mater. Interfaces* **2019**, *11*, 39424.
[121] J. E. Park, H. Nam, J. S. Hwang, S. Kim, S. J. Kim, S. Kim, J. S. Jeon, M. Yang, *Adv. Healthcare Mater.* **2024**, *13*, 2402038.
[122] H. Shin, B. H. Choi, O. Shim, J. Kim, Y. Park, S. K. Cho, H. K. Kim, Y. Choi, *Nat. Commun.* **2023**, *14*, 1644.
[123] X. Liu, Y. Wang, Y. Peng, J. Shi, W. Chen, W. Wang, X. Ma, *ACS Nano* **2023**, *17*, 24343.
[124] J. Penders, I. J. Pence, C. C. Horgan, M. S. Bergholt, C. S. Wood, A. Najer, U. Kauscher, A. Nagelkerke, M. M. Stevens, *Nat. Commun.* **2018**, *9*, 4256.
[125] J. Penders, A. Nagelkerke, E. M. Cunnane, S. V. Pedersen, I. J. Pence, R. C. Coombes, M. M. Stevens, *ACS Nano* **2021**, *15*, 18192.
[126] H. Ding, Z. Chen, *Nanotheranostics* **2021**, *5*, 461.
[127] D. Cheng, R. Liu, K. Hu, *Front. Chem.* **2022**, *10*, 958626. .
[128] M. Zhou, X. Du, H. Wang, R. Jin, *ACS Nano* **2021**, *15*, 13980.
[129] S. M. van de Looij, E. R. Hebels, M. Viola, M. Hembury, S. Oliveira, T. Vermonden, *Bioconjug. Chem.* **2021**, *33*, 4.
[130] P. Londoño-Larrea, J. P. Vanegas, D. Cuaran-Acosta, E. Zaballos-García, J. Pérez-Prieto, *Chem. Eur. J.* **2017**, *23*, 8137.
[131] W. Yang, S. Wang, X. Wei, Z. Feng, G. Qin, J. Mao, Z. Zhen, X. Miao, Y. Cheng, X. Wang, F. Huang, H. He, *Inorg. Chem. Front.* **2024**, *11*, 6396.
[132] D. M. Chevrier, L. Raich, C. Rovira, A. Das, Z. Luo, Q. Yao, A. Chatt, J. Xie, R. Jin, J. Akola, P. Zhang, *J. Am. Chem. Soc.* **2018**, *140*, 15430.
[133] O. J. H. Chai, Z. Wu, J. Xie, *J. Phys. Chem. Lett.* **2021**, *12*, 9882.
[134] Y. Chen, M. Zhou, Q. Li, H. Gronlund, R. Jin, *Chem. Sci.* **2020**, *11*, 8176.
[135] T. Y. Hou, F. Y. Shao, Y. T. Sun, K. S. Yang, W. H. Chang, C. A. J. Lin, *Nanoscale* **2020**, *12*, 17786.
[136] Y. Zhou, X. Shi, L. Ma, Y. Chai, R. Yuan, *Sens. Actuators B Chem* **2023**, *382*, 133518.
[137] M. Sugiuchi, J. Maeba, N. Okubo, M. Iwamura, K. Nozaki, K. Konishi, *J. Am. Chem. Soc.* **2017**, *139*, 17731.
[138] G. Pramanik, J. Humpolickova, J. Valenta, P. Kundu, S. Bals, P. Bour, M. Dracinsky, P. Cigler, *Nanoscale* **2018**, *10*, 3792.
[139] Z. Wu, Q. Yao, O. J. H. Chai, N. Ding, W. Xu, S. Zang, J. Xie, *Angew. Chem. Int. Ed.* **2020**, *59*, 9934.
[140] M. S. Devadas, V. D. Thanthirige, S. Bairu, E. Sinn, G. Ramakrishna, *J. Phys. Chem. C* **2013**, *117*, 23155.
[141] K. L. D. M. Weerawardene, C. M. Aikens, *J. Am. Chem. Soc.* **2016**, *138*, 11202.
[142] J. Xu, J. Li, W. Zhong, M. Wen, G. Sukhorukov, L. Shang, *Chin. Chem. Lett.* **2021**, *32*, 2390.
[143] Y. Lin, P. Charchar, A. J. Christofferson, M. R. Thomas, N. Todorova, M. M. Mazo, Q. Chen, J. Doutch, R. Richardson, I. Yarovsky, M. M. Stevens, *J. Am. Chem. Soc.* **2018**, *140*, 18217.
[144] Y. Zhong, J. Zhang, T. Li, W. Xu, Q. Yao, M. Lu, X. Bai, Z. Wu, J. Xie, Y. Zhang, *Nat. Commun.* **2023**, *14*, 658.
[145] Q. Li, D. Zhou, J. Chai, W. Y. So, T. Cai, M. Li, L. A. Peteanu, O. Chen, M. Cotlet, X. Wendy Gu, H. Zhu, R. Jin, *Nat. Commun.* **2020**, *11*, 2897.
[146] J. Xie, Y. Zheng, J. Y. Ying, *J. Am. Chem. Soc.* **2009**, *131*, 888.
[147] T. Wang, D. Xiao, *Mikrochim Acta.* **2021**, *188*, 193.

[148] V. Jain, S. Bhagat, S. Singh, *Sens Actuators B Chem* **2021**, *327*, 128886.
[149] C. Ding, Y. Xu, Y. Zhao, H. Zhong, X. Luo, *ACS Appl. Mater. Interfaces* **2018**, *10*, 8947.
[150] S. M. Lystvet, S. Volden, G. Singh, M. Yasuda, O. Halskau, W. R. Glomm, *RSC Adv.* **2012**, *3*, 482.
[151] N. Y. Hsu, Y. W. Lin, *New J. Chem.* **2016**, *40*, 1155.
[152] Y. Yue, T. Y. Liu, H. W. Li, Z. Liu, Y. Wu, *Nanoscale* **2012**, *4*, 2251.
[153] A. Aires, I. Llarena, M. Moller, J. Castro-Smirnov, J. Cabanillas-Gonzalez, A. L. Cortajarena, *Angew. Chem., Int. Ed.* **2019**, *58*, 6214.
[154] A. L. Cortajarena, A. Aires, A. Sousaraei, M. Möller, J. Cabanillas-Gonzalez, *Nano Lett.* **2021**, *21*, 9347.
[155] J. Xie, Y. Zheng, J. Y. Ying, *Chem. Commun.* **2010**, *46*, 961.
[156] H. Kawasaki, K. Yoshimura, K. Hamaguchi, R. Arakawa, *Anal. Sci.* **2011**, *27*, 591.
[157] H. Wei, Z. Wang, L. Yang, S. Tian, C. Hou, Y. Lu, *Analyst* **2010**, *135*, 1406.
[158] L. Yan, Y. Cai, B. Zheng, H. Yuan, Y. Guo, D. Xiao, M. M. F Choi, *J. Mater. Chem.* **2011**, *22*, 1000.
[159] C. L. Liu, H. T. Wu, Y. H. Hsiao, C. W. Lai, C. W. Shih, Y. K. Peng, K. C. Tang, H. W. Chang, Y. C. Chien, J. K. Hsiao, J. T. Cheng, P. T. Chou, *Angew. Chem. Int. Ed.* **2011**, *50*, 7056.
[160] H. Kawasaki, K. Hamaguchi, I. Osaka, R. Arakawa, *Adv. Funct. Mater.* **2011**, *21*, 3508.
[161] Y. Chen, J. Qiao, Q. Liu, M. Zhang, L. Qi, *Anal. Chim. Acta* **2018**, *1026*, 133.
[162] F. Wen, Y. Dong, L. Feng, S. Wang, S. Zhang, X. Zhang, *Anal. Chem.* **2011**, *83*, 1193.
[163] H. Ding, H. Li, P. Liu, J. K. Hiltunen, Y. Wu, Z. Chen, J. Shen, *Microchim. Acta* **2014**, *181*, 1029.
[164] Y. Wang, J. T. Chen, X. P. Yan, *Anal. Chem.* **2013**, *85*, 2529.
[165] A. L. West, M. H. Griep, D. P. Cole, S. P. Karna, *Anal. Chem.* **2014**, *86*, 7377.
[166] Y. Li, Y. Cao, L. Wei, J. Wang, M. Zhang, X. Yang, W. Wang, G. Yang, *Acta Biomater.* **2020**, *101*, 436.
[167] A. Aires, I. Llarena, M. Moller, J. Castro-Smirnov, J. Cabanillas-Gonzalez, A. L. Cortajarena, *Angew. Chem.* **2019**, *131*, 6280.
[168] J. Singh, N. K. Alruwaili, A. Aodah, W. H. Almalki, S. S. Almujri, M. Alrobaian, S. O. Rab, A. A. Alanezi, E. M. Haji, M. A. Barkat, A. Sahoo, J. A. Lal, M. Rahman, *J. Drug Deliv. Sci. Technol.* **2025**, *105*, 106594.
[169] G. Liang, X. Jin, S. Zhang, D. Xing, *Biomaterials* **2017**, *144*, 95.
[170] Q. Chen, J. Chen, Z. Yang, L. Zhang, Z. Dong, Z. Liu, *Nano Res.* **2018**, *11*, 5657.
[171] Y. Kong, D. Santos-Carballal, D. Martin, N. N. Sergeeva, W. Wang, G. Liu, B. Johnson, B. Bhayana, Z. Lin, Y. Wang, X. Le Guével, N. H. de Leeuw, D. Zhou, M. X. Wu, *Mater. Today* **2021**, *51*, 96.
[172] G. Yang, X. Mu, X. Pan, Y. Tang, Q. Yao, Y. Wang, F. Jiang, F. Du, J. Xie, X. Zhou, X. Yuan, *Chem. Sci.* **2023**, *14*, 4308.
[173] Z. Yang, X. Yang, Y. Guo, H. Kawasaki, *ACS Appl. Bio Mater.* **2023**, *6*, 4504.
[174] Y. Wang, J. Chen, J. Irudayaraj, *ACS Nano* **2011**, *5*, 9718.
[175] L. Shang, L. Yang, F. Stockmar, R. Popescu, V. Trouillet, M. Bruns, D. Gerthsen, G. U. Nienhaus, *Nanoscale* **2012**, *4*, 4155.
[176] H. Ding, D. Yang, C. Zhao, Z. Song, P. Liu, Y. Wang, Z. Chen, J. Shen, *ACS Appl. Mater. Interfaces* **2015**, *7*, 4713.
[177] H. Ding, H. Li, X. Wang, Y. Zhou, Z. Li, J. K. Hiltunen, J. Shen, Z. Chen, *Chem. Mater.* **2017**, *29*, 8440.
[178] Z. Li, H. Peng, J. Liu, Y. Tian, W. Yang, J. Yao, Z. Shao, X. Chen, *ACS Appl. Mater. Interfaces* **2018**, *10*, 83.
[179] Y. Chen, D. M. Montana, H. Wei, J. M. Cordero, M. Schneider, X. Le Guével, O. Chen, O. T. Bruns, M. G. Bawendi, *Nano Lett.* **2017**, *17*, 6330.
[180] G. Guedes, K. B. Uribe, L. Martínez-Parra, A. Aires, M. Beraza, J. Ruiz-Cabello, A. L. Cortajarena, *ACS Appl. Mater. Interfaces* **2024**, *16*, 59849.
[181] R. Khandelia, S. Bhandari, U. N. Pan, S. S. Ghosh, A. Chattopadhyay, *Small* **2015**, *11*, 4075.
[182] B. N. P. Kumar, N. Puvvada, S. Rajput, S. Sarkar, M. K. Mahto, M. M. Yallapu, A. Pathak, L. Emdad, S. K. Das, R. L. Reis, S. C. Kundu, P. B. Fisher, M. Mandal, *Mol. Pharm.* **2018**, *15*, 2698.
[183] Y. Yang, S. Wang, C. Wang, C. Tian, Y. Shen, M. Zhu, *Chem. Asian J.* **2019**, *14*, 1418.
[184] M. Wang, Z. Yu, H. Feng, J. Wang, L. Wang, Y. Zhang, L. Yin, Y. Du, H. Jiang, X. Wang, J. Zhou, *J. Mater. Chem. B* **2019**, *7*, 5336.
[185] F. Zhou, B. Feng, H. Yu, D. Wang, T. Wang, J. Liu, Q. Meng, S. Wang, P. Zhang, Z. Zhang, Y. Li, *Theranostics* **2016**, *6*, 679.
[186] F. Xiao, Y. Chen, J. Qi, Q. Yao, J. Xie, X. Jiang, F. Xiao, Y. Chen, J. Qi, X. Jiang, Q. Yao, J. Xie, *Adv. Mater.* **2023**, *35*, 2210412.
[187] Z. Pang, W. Yan, J. Yang, Q. Li, Y. Guo, D. Zhou, X. Jiang, *ACS Nano* **2022**, *16*, 16019.
[188] W. Yu, R. Lin, X. He, X. Yang, H. Zhang, C. Hu, R. Liu, Y. Huang, Y. Qin, H. Gao, *Acta Pharm. Sin. B* **2021**, *11*, 2924.
[189] H. Liu, G. Hong, Z. Luo, J. Chen, J. Chang, M. Gong, H. He, J. Yang, X. Yuan, L. Li, X. Mu, J. Wang, W. Mi, J. Luo, J. Xie, X.-D. Zhang, H. Liu, J. Chen, X. Mu, J. Wang, W. Mi, X. Zhang, G. Hong, M. Gong, H. He, J. Yang, Z. Luo, X. Yuan, J. Xie, J. Chang, et al., *Adv. Mater.* **2019**, *31*, 1901015.
[190] Z. Yu, B. Musnier, K. D. Wegner, M. Henry, B. Chovelon, A. Desroches-Castan, A. Fertin, U. Resch-Genger, S. Bailly, J. L. Coll, Y. Usson, V. Josserand, *ACS Nano* **2020**, *14*, 4973.
[191] A. Baghdasaryan, H. Liu, F. Ren, R. Hsu, Y. Jiang, F. Wang, M. Zhang, L. Grigoryan, H. Dai, *Proc. Natl. Acad. Sci. USA* **2024**, *121*, 23182651.
[192] X. D. Zhang, Z. Luo, J. Chen, X. Shen, S. Song, Y. Sun, S. Fan, F. Fan, D. T. Leong, J. Xie, *Adv. Mater.* **2014**, *26*, 4565.
[193] X. Zhang, Z. Luo, J. Chen, X. Shen, S. Song, Y. Sun, S. Fan, F. Fan, D. T. Leong, J. Xie, *Adv. Mater.* **2014**, *26*, 4565.
[194] S. Moro, M. Omrani, S. Erbek, M. Jourdan, C. I. Vandekerckhove, C. Nogier, L. Vanwonterghem, M. C. Molina, P. Bernadó, A. Thureau, J. L. Coll, O. Renaudet, X. Le Guével, V. Faure, *Small Sci.* **2025**, *5*, 2400156.
[195] Q. Y. Liang, C. Wang, H. W. Li, D. Y. Qi, Y. Wu, *J. Mol. Liq.* **2023**, *377*, 121516.
[196] Y. Chen, L. Xue, Q. Zhu, Y. Feng, M. Wu, *Front. Chem.* **2021**, *9*, 750404.
[197] H. M. Gil, T. W. Price, K. Chelani, J. S. G. Bouillard, S. D. J. Calaminus, G. J. Stasiuk, *iScience* **2021**, *24*, 102189.
[198] N. Sharma, W. Mohammad, X. Le Guével, A. Shanavas, *Chem. Biomed. Imag.* **2024**, *2*, 462.

David Esporrín earned his Ph.D. in Applied Chemistry from the University of the Basque Country and POLYMAT, San Sebastián, Spain, in 2022. He also graduated with a Chemistry degree and a Master's in Nanomaterials from the University of Zaragoza. He is currently a postdoctoral researcher at IBEC in the Smart Nano-Bio-Devices group. His work focuses on organic-based nanomotors with enhanced biocompatibility and mobility in viscous matrices for biomedical use. He was recently awarded an AECC fellowship to develop anisotropic gold nanoparticle-powered nanomotors for bladder cancer photothermal therapy. During his PhD, he developed an ultra-thin nanogel coating technology to improve nanoparticle stability.

Juan Fraire obtained his Ph.D. in Chemistry (2016, Argentina) and completed postdoctoral research at Ghent University, specializing in photoporation for nucleic acid delivery. He has received fellowships and grants from CONICET, Fulbright, FWO, Beatriu de Pinós–Marie Curie COFUND, and Ramón y Cajal, and was awarded the Ocean Optics Young Investigator and Sabato Institute Awards. Since 2021, he has been part of the Smart Nano-Bio-Devices group at IBEC, where he is currently Senior Researcher and leads the Gene & Light Therapies team. His work integrates nanocarrier design for nucleic acid delivery, light-triggered intracellular delivery and immunogenic activation, and self-propelled nanomotors.

Daniel Sánchez-deAlcázar earned his Ph.D. in Molecular Biology and Biomedicine from the University of the Basque Country in 2020. From 2020 to 2023, he was a postdoctoral researcher at POLYMAT, where he advanced his expertise in nanotechnology. From 2023 to 2025, he worked as a postdoctoral researcher at the Institute for Bioengineering of Catalonia (IBEC) as a Juan de la Cierva fellow, where he specialized in nanobiotechnology. In 2025, he joined Nanobots Therapeutics, a spin-off company, as a research scientist under a Torres Quevedo fellowship. His work focuses on protein engineering and the development of enzyme-driven nanomotors for biomedical applications.

Samuel Sánchez obtained his PhD in Chemistry at Autonomous University of Barcelona in 2008. Currently, he is ICREA Research Professor, Group Leader, and Deputy Director at the Institute for Bioengineering of Catalonia, Spain. Before that, he worked at the Max Planck Institute for Intelligent Systems Stuttgart, at the Institute for Integrative Nanoscience at IFW Dresden, Germany, and at MANA-NIMS in Japan. His group's main interest are new types of advanced robotics from nano- to mesoscale, including self-propelled nanoparticles as intelligent vehicles in biomedicine to the 3D Bioengineering of biohybrid robots and actuators. He is also a cofounder CSO, and CEO-interim of Nanobots Therapeutics SL.